university of groningen / faculty of science and engineering

Laser Fields for Quantum State Control of BaF Molecules

The Search for a Permanent EDM of the Electron

Author:
Sybrich VAN SCHALM
(s5390869)

Supervisor:
dr. Lorenz WILLMANN
Second examiner :
prof. Julia EVEN

Bachelor's Thesis
To fulfill the requirements for the degree of
Bachelor of Science in Physics
at the University of Groningen
in the Van Swinderen Institute for Particle Physics and Gravity

July 7, 2025

Abstract

The existence of a permanent electron electric dipole moment (eEDM) would imply violations of parity and charge-parity symmetries, offering a potential window into Beyond the Standard Model (BSM) physics. The NL-eEDM experiment aims to improve the current upper bound on the eEDM by conducting a spin precession measurement on a cold beam of barium monofluoride (BaF) molecules. It is the first experiment in the field to employ laser light counterpropagating to the molecular beam for coherent quantum state control, enabling improved spatial and temporal precision in two-photon transitions. This thesis focuses on the characterization and optimization of the counterpropagating laser system by minimizing optical power losses, optimizing acousto-optic modulator (AOM) performance, and monitoring laser power stability. High and stable intensity is essential for achieving high-fidelity quantum state manipulation. Systematic measurements revealed no anomalous power losses across the optical configuration, and the delivered intensity was found sufficient for strong interaction with the molecular beam. Although intensity fluctuations were observed over multi-day timescales, these are unlikely to affect coherence during individual measurement cycles. For long-term statistical data collection, however, continuous monitoring is recommended to enable correction during data analysis. Together, these results demonstrate the reliability of the counterpropagating laser system and support the NL-eEDM experiment in its objective of improving experimental sensitivity to symmetry-violating effects in fundamental physics.

Contents

1 The eEDM as a Probe of New Physics

The Standard Model (SM) of particle physics is a phenomenally successful framework in modern science [1]. It systematically classifies the known fundamental particles and describes their interactions through three of the four fundamental forces: the electromagnetic, weak, and strong interactions. Despite its predictive power in laboratory experiments [2], the SM is widely regarded as incomplete. Most notably, it does not incorporate gravity, the dominating force on cosmological scales, into its theoretical structure [3]. Attempts to unify all four fundamental forces have led to theoretical extensions of the SM [4], collectively referred to as Beyond the Standard Model (BSM) physics [5]. These extensions, such as supersymmetry (SUSY), attempt to address shortcomings by introducing new particles and interactions [6]. Many of them predict substantial violations of fundamental symmetries [7]: phenomena that can be tested experimentally.

Symmetry principles lie at the heart of the SM and underpin our understanding of physical laws [8]. Among them, the three discrete symmetries of charge conjugation (C), parity (P), and time reversal (T) are of particular interest. The SM permits violations of C and P individually, as well as of CP in certain weak interactions [9], though these effects are tightly constrained. According to the CPT theorem, the combined symmetry of charge, parity, and time reversal (CPT) must be strictly conserved in the SM [1]. Under this assumption, observing T violation is equivalent to observing CP violation. Detecting such violations at levels beyond Standard Model predictions would provide compelling evidence for its incompleteness [10].

Two complementary experimental strategies are used to probe symmetry violations. High-energy collider experiments, such as those conducted at LHCb, search for CP violation through the direct creation of new particles [11]. In parallel, precision measurements in atomic and molecular systems use the permanent electron electric dipole moment (eEDM) as a sensitive probe [10]. Classically, a nonzero eEDM implies a separation of positive and negative charge along the spin axis of the electron, violating P and T symmetries and, by extension, CP symmetry [6]. While the Standard Model predicts an eEDM of less than 10^{-38} e cm [12], which is far below current experimental sensitivity, many BSM theories allow values several orders of magnitude larger and within measurable range [10]. Consequently, improving experimental limits on the eEDM offers a powerful test of new physics.

Recent advances in molecular beam experiments have significantly tightened the upper bound on the eEDM. In 2018, the ACME collaboration used thorium monoxide (ThO) molecules to set a limit of $|d_e| < 1.1 \cdot 10^{-29}$ e cm [13]. This was surpassed in 2023 by experiments with trapped hafnium fluoride ions (HfF^+), which further constrained the eEDM to $|d_e| < 4.1 \cdot 10^{-30}$ e cm [14]. New techniques are continuously being developed to improve sensitivity. By potentially surpassing the 10^{-30} e cm threshold, these experiments extend beyond the reach of current high-energy collider experiments [6].

The NL-eEDM experiment aims to further tighten the upper bound on the eEDM using a cold molecular beam of barium monofluoride (BaF) [6]. As a spin precession experiment, it prepares the molecules in a coherent superposition of spin states and allows them to evolve in precisely controlled electric and magnetic fields. A nonzero eEDM would induce a measurable phase shift upon reversal of the electric field. The NL-eEDM experiment is the first experiment in the field to employ laser light counterpropagating with the molecular beam for quantum state transfer, offering improved spatial and temporal control. Central to this approach is the use of precisely timed laser pulses to drive two-photon transitions in the molecular spin states.

This thesis focuses on the systematic aspects of the counterpropagating laser system, rather than on long-term statistical data collection. Specifically, it involves characterizing and optimizing the optical configuration by minimizing power losses, optimizing acousto-optic modulator (AOM) performance, and monitoring the stability of laser parameters. These objectives contribute to the reliability of the laser system, ultimately supporting the broader experimental effort of pushing the sensitivity of eEDM searches to new limits.

2 Experimental Search for an eEDM

The search for an electron electric dipole moment (eEDM) is a powerful low-energy probe for Beyond the Standard Model physics. This section provides an overview of the theoretical principles underlying eEDM measurements and describes the experimental strategies pursued to detect such a small effect. Particular emphasis is placed on the methodology of the NL-eEDM experiment, which employs an innovative laser system for precise quantum state control in its aim for high experimental sensitivity.

2.1 Theoretical Framework

An electric dipole moment (EDM) is a polar vector quantity that characterizes the separation between positive and negative electric charges. In classical physics, an EDM arises from a system consisting of a charge $+q$ and an opposite charge $-q$ separated by a displacement vector $\vec{r}$, leading to an EDM $\vec{d} = q\vec{r}$ [15]. However, in the context of elementary particles such as electrons, which are considered point-like quantum systems, there is no meaningful separation $\vec{r}$. The classical picture therefore breaks down. Instead, the EDM must be defined with respect to the only intrinsic vector quantity available: the particle spin $\vec{S}$ [1]. Due to rotational symmetry, any EDM component perpendicular to the spin axis would average to zero. If a permanent EDM exists, it must be aligned along the spin axis. However, this leads directly to violations of both P and T symmetries [15]. Under P or T transformation, the EDM vector $\vec{d}$ reverses direction relative to the spin $\vec{S}$, while magnetic dipole moment $\vec{\mu}$ remains unchanged [16] as shown in figure 1. The disrupted alignment between $\vec{d}$ and $\vec{S}$ means that a nonzero EDM cannot exist without breaking fundamental symmetries.

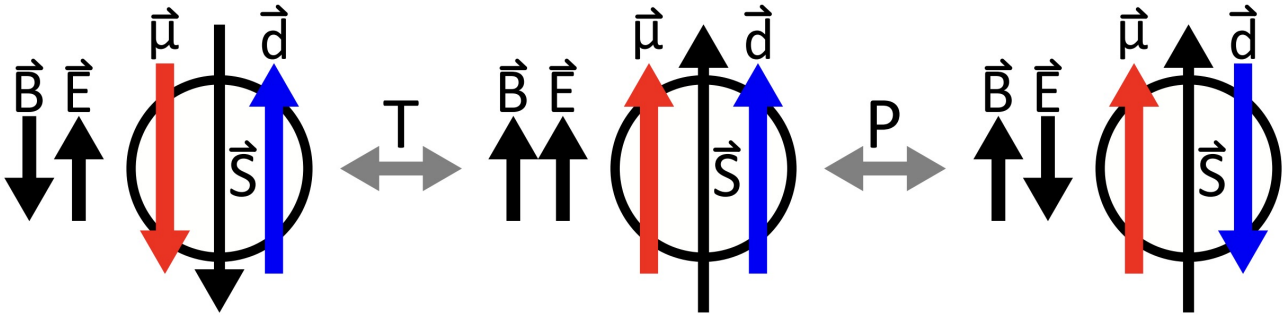

Figure 1: A permanent electric dipole moment (EDM) violates P and T symmetries, because it requires a fixed alignment between EDM vector $\vec{d}$ and particle spin $\vec{S}$, which transform differently under P and T operations. Parity transformation P reverses the spatial coordinate system of the particle, and thereby the directions of $\vec{d}$ and electric field $\vec{E}$. Time transformation T reverses the direction of time, and thereby that of $\vec{S}$, magnetic field $\vec{B}$, and magnetic dipole moment $\vec{\mu}$. Figure extracted from [1].

The interaction of an electron with external electric and magnetic fields through its intrinsic dipole moments is described by the Hamiltonian

$$H_{\pm} = -(\vec{\mu}\vec{B} \pm \vec{d}\vec{E}) \tag{1}$$

where $\vec{\mu} = \mu\vec{S}$, $\vec{d} = d\vec{S}$, and the sign of the EDM term depends on whether electric field $\vec{E}$ and magnetic field $\vec{B}$ are aligned (+) or anti-aligned (-) [1]. In typical experimental regimes, the magnetic dipole

interaction $\vec{\mu}\vec{B}$ dominates over the electric dipole interaction $\vec{d}\vec{E}$, making the latter a tiny symmetry-violating perturbation to a larger, well-understood Hamiltonian. As such, its detection requires a precision experiment. If P and T symmetries were strictly conserved, particles with spin would exhibit degenerate energy states corresponding to EDMs aligned both parallel and antiparallel to the spin axis. Since such degeneracy is not allowed by the observed structure of elementary particles, detection of a nonzero eEDM would imply violations of fundamental symmetries [15].

To probe the eEDM experimentally, one can examine how the electron spin behaves in the presence of strong, well-controlled electric and magnetic fields. A central technique involves applying electric field $\vec{E}$ either parallel or antiparallel to magnetic field $\vec{B}$ [15]. In such a setup, the electron spin precesses about the field axis with frequency ω, leading to an energy splitting $\Delta E = \hbar\omega$ between the spin states aligned parallel and antiparallel to the electric field. The presence of an EDM slightly shifts this frequency, which is given by

$$\omega_{\pm} = \frac{2(\vec{\mu}\vec{B} \pm \vec{d}\vec{E})}{\hbar}, \tag{2}$$

[17]. The dot products between each dipole moment and its corresponding field yield scalar energy contributions that depend on the angle between the two vectors. Maximum interaction energy occurs when the dipole and field are aligned or anti-aligned, while it is zero for orthogonal configurations. In spin-$\frac{1}{2}$ systems, this leads to two distinct energy eigenstates, spin-up and spin-down, corresponding to alignment and anti-alignment with the external field. For higher-spin systems, such as spin-1 particles, the situation becomes more complex. This is discussed in detail in [18].

Most EDM experiments rely on detecting a phase shift in the spin precession of a particle [19]. The accumulated phase difference ϕ between the spin states is

$$\phi_{\pm} = \omega_{\pm} T, \tag{3}$$

where T is the interaction time of the particle with the applied electric and magnetic fields. At the start of the interaction time, a coherent superposition of the two spin states is prepared. As the particle interacts with the fields, this superposition evolves, accumulating a phase that is proportional to the induced relative energy shift between the spin states [19]. At the end of the interaction time, the spin state is projected onto a measurement basis, allowing the accumulated phase to be read out [6].

By reversing the direction of the electric field relative to the magnetic field and measuring the corresponding change in phase, the EDM contribution can be isolated as

$$d = \frac{\hbar\Delta\phi}{4ET}, \tag{4}$$

where $\Delta\phi = \phi_{+} - \phi_{-}$. This differential measurement relies on the idea that field reversal cancels all systematic effects that potentially mimic EDM signals [17]. A differential measurement is advantageous since $\mu B >> dE$, making it otherwise challenging to distinguish the small eEDM signal from the dominant magnetic background [20]. Moreover, it allows the EDM contribution to be extracted directly from a single phase difference, rather than requiring two separate absolute energy measurements.

A particularly promising approach to enhance the sensitivity of eEDM measurements is to use polar molecules, which possess large internal electric fields [19]. In certain paramagnetic diatomic molecules containing heavy atoms, the presence of a valence electron with an EDM leads to a molecular EDM orders of magnitude larger than the bare eEDM [10]. These enhancements, that can go up to a value of 10^6, arise from relativistic effects near the heavy nucleus [21], the scalar-pseudoscalar (S-PS) interaction between the electrons and nucleons [7], and the close-lying rotational levels of opposite parity [10]. As such, these molecules serve as powerful amplifiers for detecting tiny symmetry-violating effects [6].

2.2 NL-eEDM Experiment

Achieving high sensitivity in an eEDM measurement involves a combination of careful molecular selection, coherent quantum state preparation, and manipulation of molecular populations. This subsection outlines the core components of the experimental approach of the NL-eEDM experiment: from the rationale behind choosing barium monofluoride as the molecular probe, to the mechanism by which spin precession is regulated.

2.2.1 Use of Barium Monofluoride (BaF) Molecules

Various molecules are used in ongoing eEDM experiments to enhance the effective electric field. Although BaF has a smaller enhancement factor compared to molecules like YbF and ThO, its lower mass allows for more efficient beam deceleration [6]. This results in a longer interaction time T between the molecules and the applied fields, thereby increasing the accumulated phase difference ϕ and improving sensitivity to an eEDM [15]. Extended interaction time is a major advantage of the NL-eEDM experiment [6]. In addition, the electronic ground state of BaF offers a suitable structure for efficient laser cooling and detection [6]. The experiment uses molecules in the $X^2\Sigma^+$ state, labeled by rotational level $N = 0$, vibrational level $v = 0$, and hyperfine level $F = 1$ [20]. Within this hyperfine level, a superposition is created of two hyperfine substates ($m_F = \pm 1$), which have their spin oriented in opposite directions [10]. These two spin states gain a phase difference, as described in section 2.1, when influenced by the applied electric and magnetic fields. This phase difference is read out when the superposition is projected onto the $N = 0$, $F = 0$ state, which serves as the measurement basis. The $N = 0$ state is favored in part due to its polarization factor, which supports the substantial degree of polarization needed for a measurable eEDM effect [10].

2.2.2 Measurement Principle of the Spin Precession Experiment

Figure 2 gives a schematic overview of the experimental setup used in the NL-eEDM experiment. The spin precession takes place in the interaction zone, which is magnetically shielded to ensure a stable and homogeneous magnetic environment. Inside the five-layer μ-metal shield, cosine coils generate a magnetic field of $B \approx 8$ nT. To suppress environmental magnetic noise, three orthogonal pairs of Helmholtz-like coils are placed around the setup to provide compensation, resulting in a total shielding factor of $\Delta B_{ext}/\Delta B_{int} \approx 10^6$. Two parallel glass plates, coated with the conductive material indium-tin-oxide (ITO), generate a uniform electric field of $E = 10$ kV/cm. The usable length of these plates is $l = 65$ cm, allowing the BaF molecules to have a spin precession time of $T = 1$ *ms*. [17]

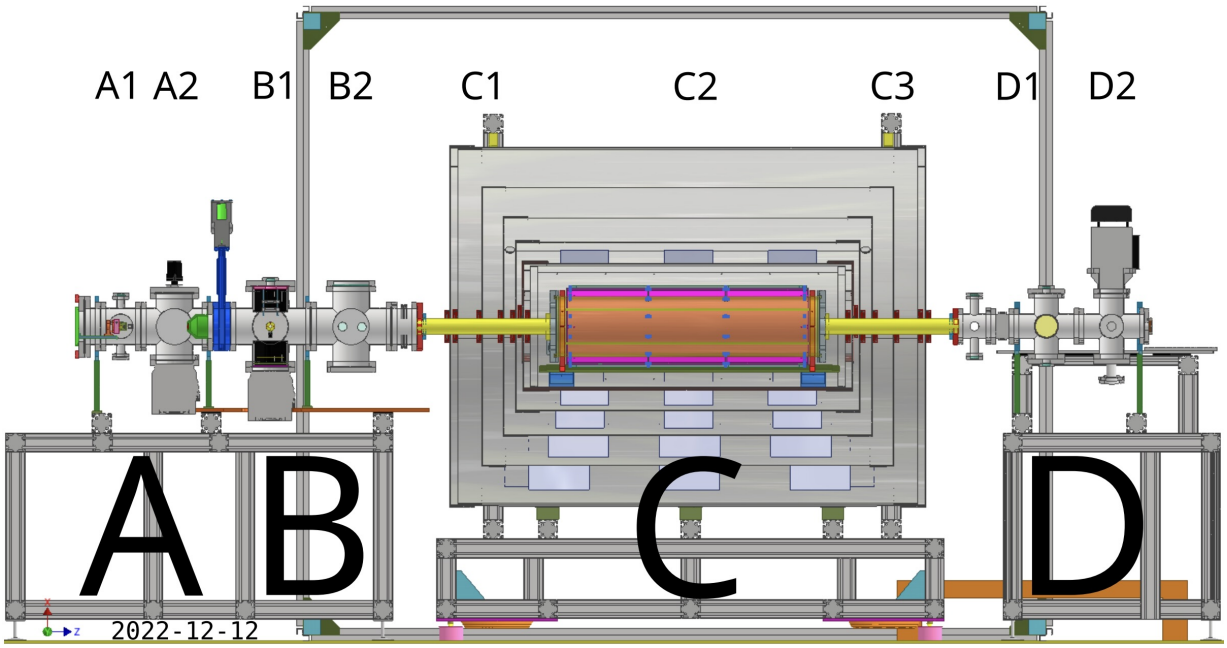

Figure 2: Full setup of the NL-eEDM experiment. In Section A, a cryogenic buffer gas source produces a BaF molecular beam that travels from the left to the right through the setup. In Section B, the molecules are prepared for the start of the spin precession experiment. At B1, the number of molecules is probed for normalisation purposes. At B2, the molecular quantum states are pumped to a well-defined start of the spin precession. Section C2 is the magnetically shielded interaction zone, where the molecules interact with controlled magnetic and electric fields, inducing spin precession. The molecular beam can enter and exit this interaction zone via titanium tubes in Sections C1 and C3, respectively. The final state of the molecules is read out in Section D using fluorescence detection. Figure extracted from [1].

This thesis focuses on the quantum state control of BaF molecules inside the interaction zone. The NL-eEDm experiment is the first experiment in the field to employ a laser system counterpropagating to the molecular beam for quantum state control, marking a significant methodological advancement [20]. A description now follows of the individual state manipulations involved in the spin precession experiment. Quantum states are denoted using the Dirac notation $|F,m_F\rangle$, labeled by total angular momentum F and its projection m_F.

Before entering the interaction zone, the molecules are prepared in the $|F,m_F\rangle = |0,0\rangle$ hyperfine sublevel of the $X^2\Sigma, N = 0$ groundstate. This state preparation creates a well-defined start of the spin precession [1], which takes place in the controlled electric and magnetic fields of the 0.5-m-long interaction zone. Assuming total population transfer, the initial state of the experiment is $|\psi(0)\rangle = |0,0\rangle$ [17].

Once the molecules are within the homogeneous field region, the aim is to fully transfer the molecular population from the initial state to the bright superposition $|x\rangle = \frac{1}{\sqrt{2}}(|1,-1\rangle + |1,+1\rangle)$ using a laser light pulse [20]. Such a transfer is called a π-pulse and can be achieved when the laser light is polarized such that the initial state is coupled to the bright superposition $|x\rangle$ rather than to the dark superposition $|y\rangle = \frac{1}{\sqrt{2}}(|1,-1\rangle - |1,+1\rangle)$. To drive the transition from the $F = 0$ state to the desired $F = 1$ superposition, the NL-eEDM experiment uses a two-photon process: two laser beams, E and F,

with slightly different frequencies are combined into a single beam and directed to counterpropagate the molecular beam [20]. Figure 3 shows an energy level diagram of the transitions used to undertake this two-photon process. Ideally, the lasers are off-resonance and their frequency difference is close to the hyperfine splitting between the $F = 0$ and $F = 1$ levels of the BaF ground state [17]. Both lasers are pulsed on simultaneously to interact with the molecules as they enter the interaction zone, where the spin precession begins [1].

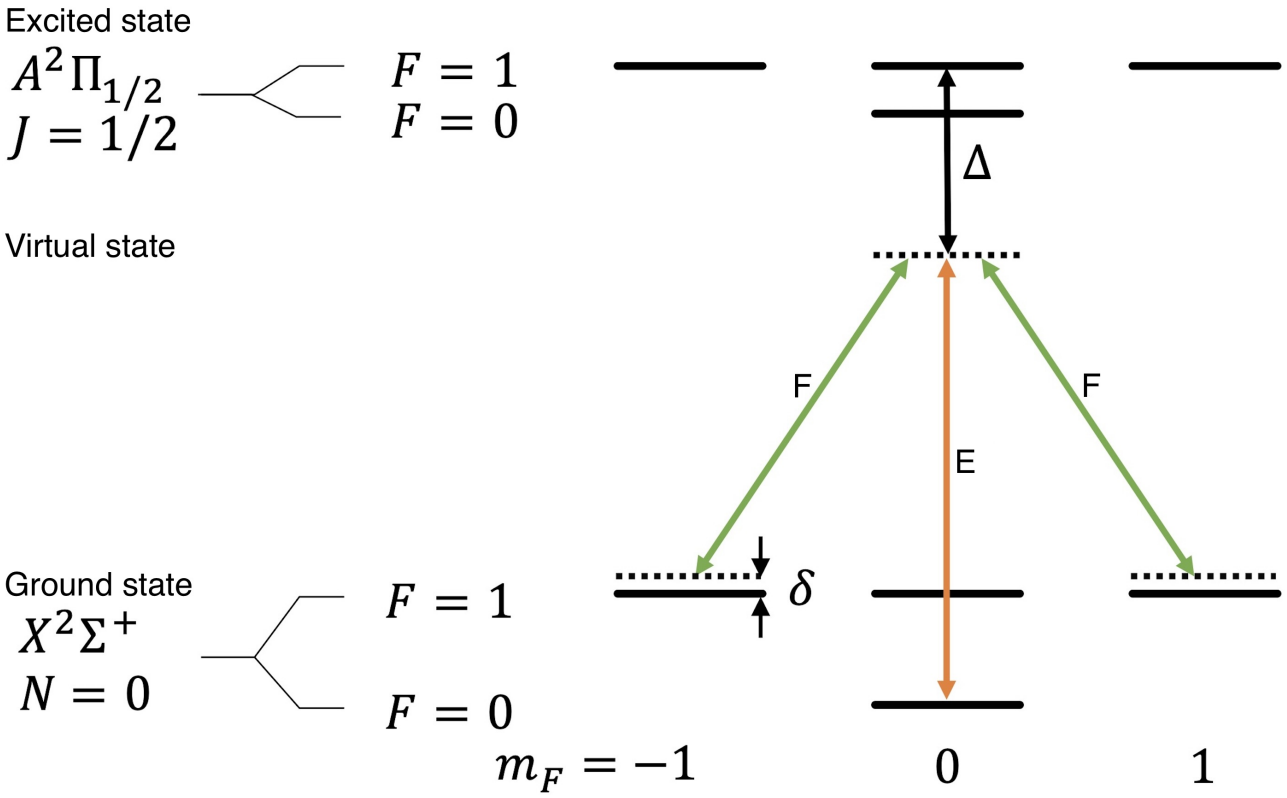

Figure 3: Energy level diagram showing the two-photon transition used for quantum state transfer from the $|0,0\rangle$ sublevel to a $|1,\pm1\rangle$ superposition within the $X^2\Sigma, \nu = 0, N = 0$ ground state of BaF. The transition is driven by the light fields of two lasers, labeled E and F, which have a frequency difference matched to the hyperfine splitting in the ground state. Each laser is detuned by $\Delta = 1$ GHz from the electronically excited state $A^2\Pi_{\frac{1}{2}}, \nu = 0, J = \frac{1}{2}$. The two-photon detuning δ is on the order of several KHz. Figure adapted from [18].

During the precession period, the molecules have free evolution in the electric and magnetic fields. The precession of the superposition creates different phases, described by equation 3, for the two spin states. Assuming a perfect π-pulse, the molecular population after precession time T is described by

$$|\psi(T)\rangle = cos\left(\frac{\phi}{2}\right)|x\rangle - isin\left(\frac{\phi}{2}\right)|y\rangle, \tag{5}$$

where ϕ is the phase gained during precession, and $|x\rangle$ and $|y\rangle$ are the bright and dark states of the superposition, respectively [20]. This demonstrates that ψ evolves periodically between the bright and dark superposition states at a frequency described by equation 2.

After the precession time, a second laser pulse with identical parameters to the first is applied to recouple the bright state $|x\rangle$ to the $|0,0\rangle$ sublevel. This second pulse selectively addresses the bright

state, leaving the dark state $|y\rangle$ unaffected and remaining in the $F = 1$ level [17]. The resulting state of the system is

$$|\psi(T+t)\rangle = cos\left(\frac{\phi}{2}\right)|0,0\rangle - isin\left(\frac{\phi}{2}\right)|y\rangle, \tag{6}$$

where t is the duration of the laser pulse.

The readout extracts phase information by measuring the populations in the $F = 0$ and $F = 1$ levels. Assuming perfect π-pulses, the probabilities of finding the molecules in each hyperfine state are

$$P_{F=1} = sin^2\left(\frac{\phi}{2}\right) \tag{7}$$

and

$$P_{F=0} = cos^2\left(\frac{\phi}{2}\right). \tag{8}$$

The readout measurements are performed after the molecules exit the interaction zone and are exposed to detection light in a designated chamber [20]. Reversing the direction of the electric field relative to the magnetic field causes a sign change in the eEDM-induced contribution to the accumulated phase ϕ, resulting in a measurable difference in the observed populations $P_{F=1}$ and $P_{F=0}$. This enables the eEDM signal to be isolated from other, non-reversing effects.

2.2.3 Rabi Frequency in Quantum State Control

Rabi frequency describes the rate at which molecules oscillate between two quantum states when driven by a laser pulse. Coherent state transfer relies on the application of perfect π-pulses, which correspond to a Rabi phase $\phi_R = \pi$ gained during the laser interaction time. This ensures the bright state $|x\rangle$ is fully populated by the laser pulse before free evolution starts. A molecular phase accumulation of $\phi = \pi$ during spin precession results in a state rotation from $|x\rangle$ to $|y\rangle$. Since the dark state $|y\rangle$ is decoupled from the second laser pulse, no molecules are transferred back to the ground state. In this ideal scenario, the measured populations are $P_{F=1} = 1$ and $P_{F=0} = 0$ [17]. However, under experimental conditions, a perfect π-pulse is not realisable [20], leading to incomplete population transfer.

A key experimental parameter influencing the laser pulses is the total laser intensity of the counterpropagating beams used for the two-photon transition described in section 2.2.2. The sensitivity of population transfer to the intensity of a single laser i can be quantified using Rabi frequency

$$\Omega_i = \sqrt{\frac{\Gamma_i^2}{2I_{i,sat}}} \cdot \sqrt{I_i}, \tag{9}$$

where Γ_i is the decay rate of the driven transition, and $I_{i,sat}$ is the saturation intensity describing the electric field strength of the light. The relevant values are $\Gamma = \frac{1}{57}$ ns^{-1} and $I_{sat} \sim 0.6$ mW/cm^2 [17]. Since intensity is related to power by $I = \frac{P}{A}$, where A is the beam area, equation 9 can be rewritten in terms of power as

$$\Omega_i(P) = K\sqrt{P} \text{ with } K = \sqrt{\frac{\Gamma_i^2}{2I_{i,sat}A}}. \tag{10}$$

Assuming a circular beam with radius $r = 20 \pm 2$ mm [17], the area of the expanded counterpropagating beam is approximated as $A = \pi r^2 = \pi \cdot 20^2$ mm^2 $= (1.3 \pm 0.3) \cdot 10^3$ mm^2.

The two-photon transition governed by the counterpropagating laser beams has a two-photon Rabi frequency of

$$\Omega_{EF} = \frac{\Omega_E \Omega_F}{2\Delta}, \tag{11}$$

where Ω_E and Ω_F are the single-photon Rabi frequencies of lasers E and F, respectively, and Δ is the detuning from the intermediate excited state [20]. This two-photon Rabi frequency in turn determines the Rabi phase ϕ_R, which is given by

$$\phi_R = \Omega_{EF} t, \tag{12}$$

where t is the pulse duration [20]. Assuming a fixed pulse duration $t = 50\mu s$ [17], a perfect π-pulse would require

$$\Omega_{EF} = \frac{\pi}{50\mu s} = 2\pi \cdot 10^4 \text{ Hz}. \tag{13}$$

Any deviation from a Rabi phase $\phi_R = \pi$ modifies the final population values at the readout state. If uncorrected, this results in a systematic shift of the extracted eEDM contribution.

3 Counterpropagating Laser Fields

To enable precise quantum state manipulation for a succesful eEDM measurement, the NL-eEDM experiment employs a counterpropagating laser system. This section outlines its design and performance considerations, focusing on the optical components and alignment strategies that ensure stable, efficient light delivery to the molecular beam. By addressing both theoretical principles and practical implementation, it lays the groundwork for understanding how the counterpropagating laser contributes to a reliable spin precession measurement.

3.1 Research Motivation and Objectives

The NL-eEDM experiment relies entirely on optical techniques to perform the spin precession measurement [17]. Laser pulses counterpropagating to the molecular beam allow for improved temporal control, which in turn contributes to the consistency of the applied π-pulses [20] as seen in equation 12. Any deviation from perfect π-pulses leads to imperfect population transfer, ultimately affecting the accuracy of the final readout. This motivates a detailed investigation of the counterpropagating laser system, with the aim of optimizing its parameters and identifying potential systematic effects that could influence the extraction of the eEDM signal.

Besides precise timing, maintaining a nearly constant two-photon Rabi frequency is essential for producing ideal π-pulses. This consideration places several demands on the optical configuration of the counterpropagating laser. The laser beams involved in the two-photon transition must have a well-defined frequency difference, matching the hyperfine splitting of the BaF spin states. Their polarizations must be orthogonal to avoid interference and to enable recombination via a polarizing beam splitter. There cannot be a relative phase difference between the beams, since a phase offset would change the projection of the superposition state back onto the measurement basis, thereby altering the observed signal. Furthermore, the beams must be well-overlapped and spatially broad enough to uniformly cover the molecular beam. As outlined in equations 9 and 11, a consistent two-photon Rabi frequency also relies on stable and spatially homogeneous beam intensities.

The central objective of this thesis is to characterize how the counterpropagating laser light propagates through the optical setup. Accurate characterization of power losses in the optical chain helps to ensure that enough light consistently reaches the molecules. Two acousto-optic modulators (AOMs) are implemented in the setup as they can generate the necesssary frequency difference for the two-photon transition and influence the transmission of laser power through the system. Their performance depends on proper alignment of the incoming laser beams, particularly the focusing of the Gaussian profiles into the AOM crystals, as well as on selecting acoustic drive frequencies appropriate to their central values. Using a power meter to monitor the combined beam before it reaches the molecules, potential fluctuations in intensity can be identified. These research objectives contribute to an optimized and stable laser system, supporting the overall sensitivity of the experiment.

3.2 Gaussian Beam Optics

Gaussian laser beams exhibit an intensity profile following a Gaussian function across any cross section perpendicular to the direction of propagation of the beam. This results in a bell-shaped intensity distribution that is maximum on the beam axis and decreases exponentially with radial distance. Gaussian laser beams have the smallest product of beam diameter and angular divergence of all optical beams. This makes them ideal for modeling circular apertured lasers like the counterpropagating laser in the NL-eEDM experiment, as results based on Gaussian approximations yield sufficiently accurate predictions for the behaviour of the beam through optical systems [22].

A defining feature of the Gaussian beam is its beam waist W_0, which is the location along the beam axis z where the beam radius is at its minimum. If a gaussian beam is strongly focused by a collimating lens, the radius of the beam in the focal plane is given by

$$W_0 = \frac{2f\lambda}{\pi d_l}, \tag{14}$$

where f is the focal length of the lens, λ is the wavelength of the laser and d_l is the beam diameter at the lens. To define the effective diameter of the focused Gaussian spot, it is common to use the diameter of the beam that encloses approximately 86% of the total beam power [23]. For a circularly symmetric Gaussian beam, this corresponds to twice the beam waist, leading to an effective spot size d_0 of

$$d_0 = 2W_0 = \frac{4f\lambda}{\pi d_l}. \tag{15}$$

Note that several assumptions are made to yield this dependence. The laser is considered to emit a single, well-defined wavelength and is modeled as a theoretical Gaussian beam. The focusing lens is treated as an ideal thin lens with a uniform focal length across its entire aperture. Additionally, the incident beam is assumed to be perfectly collimated on the lens, such that the beam waist is located precisely at the focal point of the lens along the optical axis.

As the beam propagates away from the waist, which is defined at $z = 0$, the beam radius $W(z)$ increases with the axial distance z following

$$W(z) = W_0\sqrt{1 + \left(\frac{z}{z_R}\right)^2}, \tag{16}$$

where z_R is the Rayleigh range

$$z_R = \frac{\pi W_0^2}{\lambda} \tag{17}$$

[24]. The Rayleigh range quantifies the distance z from the beam waist to the point where the beam radius $W(z)$ has increased by a factor of $\sqrt{2}$, doubling the cross-sectional area πW^2. The Rayleigh range thus is a measure of the distance over which the laser beam remains tightly focused. It defines the depth-of-focus (DOF) as

$$DOF = 2z_R \tag{18}$$

[24]. Figure 4 shows the side profile of a Gaussian beam and indicates its depth-of-focus. This region is particularly relevant since the beam spreads slowly within it, allowing for effective interaction with components such as AOMs.

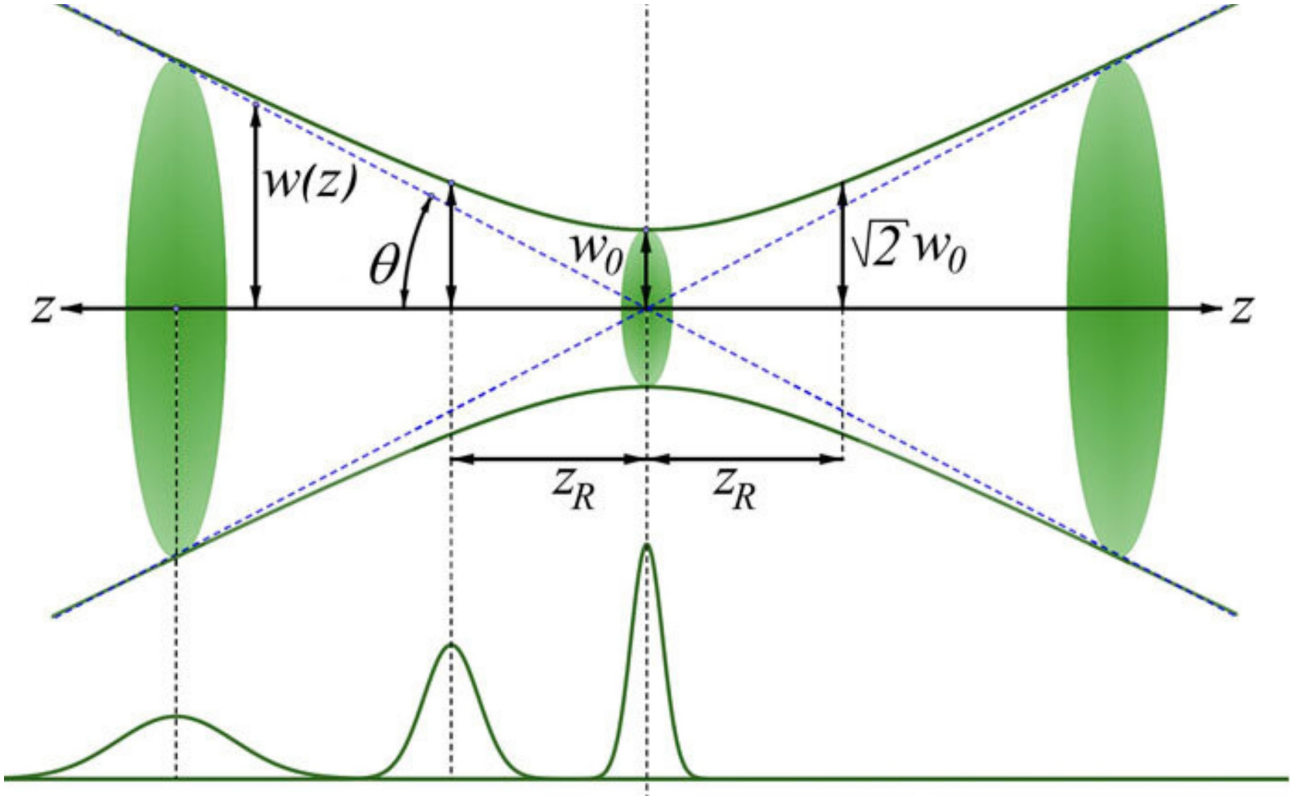

Figure 4: Visual representation of the evolution of a Gaussian beam along beam axis z, featuring its key parameters: beam waist W_0, divergence angle θ, Rayleigh range z_R and depth-of-focus $2z_R$. The depth-of-focus is defined as the region within which the beam radius $r(z)$ increases by no more than a factor of $\sqrt{2}$ relative to the beam waist. The lower part of the figure shows three projections of the Gaussian beam at different distances along z, highlighting that the narrowest profile occurs at the beam waist. Figure extracted from [25].

3.3 AOM: Acousto-Optic Modulator

An acousto-optic modulator (AOM) is a device that leverages the interaction between sound waves and light within a crystal to diffract and shift the frequency of laser beams. This phenomenon, known as the acousto-optic effect, arises from the photoelastic effect wherein the refractive index of a material is modulated by the mechanical strain of an acoustic wave [26]. In an AOM, a piezoelectric transducer is affixed to a transparent crystal. When driven by a radio-frequency (RF) signal, the transducer generates an acoustic wave that propagates through the crystal. This acoustic wave induces periodic variations in the refractive index of the crystal, effectively creating a moving diffraction grating. As a laser beam enters the crystal, it interacts with this grating, resulting in a frequency shift of the light and diffraction into a sideband. The first order sidebands are shifted by plus and minus the frequency applied at the RF input. In general, an n^{th} order beam experiences a shift of n times this frequency. Figure 5 shows a schematic representation of the working principle of an AOM.

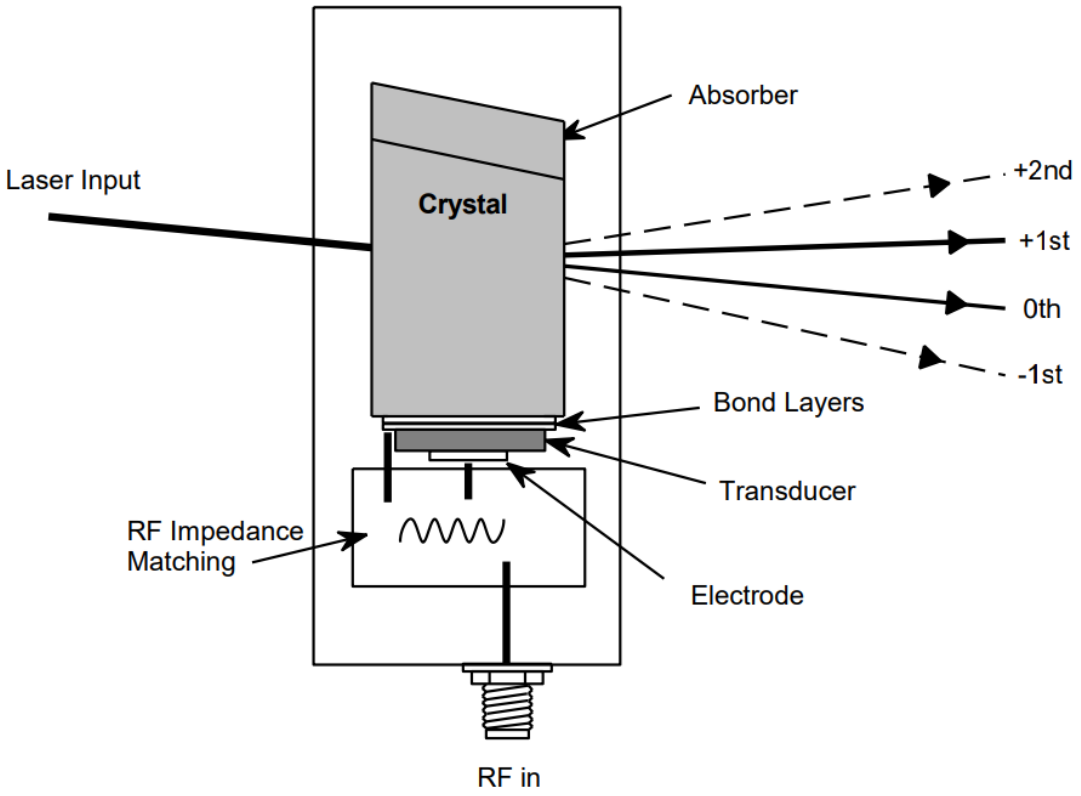

Figure 5: Schematic representation of an acousto-optic modulator (AOM). A laser beam enters a transparent crystal, where it interacts with a periodic refractive index modulation induced by an acoustic wave. This wave is generated by a piezoelectric transducer, which is driven by an RF signal applied through an electrode. The transducer, bonded to the crystal via intermediate layers, launches the acoustic wave into the medium. An impedance matching element is included to optimize the transfer of RF power. As the light interacts with the resulting moving diffraction grating, it is split into several diffracted beams, each corresponding to a different diffraction order. The n^{th} order beam experiences a frequency shift of n times the applied RF frequency. An absorber is placed at the end of the crystal to prevent acoustic reflections. Figure extracted from [27].

The diffraction efficiency (DE) of an AOM is defined as the ratio of the n^{th} order optical power P_n to the incident optical power P_{in} [26]:

$$DE = \frac{P_n}{P_{in}}. \tag{19}$$

The optical power of the diffracted beams is controlled by the acoustic power, meaning that more RF power applied to the AOM leads to more power in the diffracted beams until a saturation point is reached [27]. The NL-eEDM experiment operates AOMs in the Bragg regime, which ensures predominant diffraction into the first order sideband under conditions of phase matching between the incident light and the acoustic wave. This occurs when the interaction satisfies the Bragg condition, where the incident angle and acoustic frequency are tuned such that constructive interference maximizes diffraction into one direction. The optimal angle of incidence for efficient diffraction, known as Bragg angle θ_B, is given by

$$\theta_B = sin^{-1}\left(\frac{\lambda_o}{2\lambda_a}\right) = sin^{-1}\left(\frac{\lambda_o f}{2v_s}\right) \approx \frac{\lambda_o f}{2v_s}, \tag{20}$$

where λ_o is the optical wavelength, λ_a is the acoustic wavelength, f is the acoustic frequency, ν_s is the speed of sound in the AOM medium, and the approximation is valid under the assumption that θ_B is small [24]. For a fixed angle of incidence, only that component of the acoustic wave that satisfies this relation effectively interacts with the optical beam. Consequently, detuning the AOM from its design frequency leads to a mismatch with the Bragg condition and results in reduced diffraction efficiency. The bandwidth B of an AOM, defined as the maximum frequency range over which efficient modulation occurs, is given by

$$B = \frac{\nu_s}{D}, \tag{21}$$

where D is the diameter of the optical beam at the interaction region of the crystal [24]. Thus, the bandwidth can be increased by reducing the radius of the incident Gaussian beam at the center of the crystal. This is especially relevant when an AOM is not operated at its design frequency. Tighter beam focus also directly increases diffraction efficiency.

The efficiency of the acousto-optic interaction partly depends on the optical wavelength. The materials in the AOMs should have a high transparency at the relevant wavelengths, and reflections should be minimized with anti-reflection (AR) coatings [26]. A mismatch with the optical wavelength leads to insertion losses (IL), meaning that power is lost in the AOM device itself, following

$$IL = 1 - \frac{P_{out}}{P_{in}}, \tag{22}$$

where P_{out} is the total power exiting the AOM [27].

AOMs are used in the experiment to satisfy two requirements of the counterpropagating beams as outlined in Section 3.1: precise temporal control and accurate frequency tuning. To achieve this, the AOMs must enable fast optical switching to produce well-defined laser pulses with a duration of $t = 50\ \mu$s, marking the start and end of the spin precession interval. The switching time of the AOMs should be shorter than 50 ns [28]. Additionally, the AOMs must allow fine frequency tuning. The frequency difference within the counterpropagating beam should match the hyperfine splitting of the BaF spin states, which is measured to be 65.848714(40) MHz [20]. To achieve KHz-level control over the two-photon detuning δ, which sets how close the frequency difference in the combined beam is to hyperfine resonance, the AOMs must offer a tuning resolution of approximately $\pm$20 kHz [28].

3.4 Optical Configuration

A two part optical configuration is set up to guide the counterpropagating amplified diode laser from its fiber optic output to the molecular beam. In the first part, shown in figures 6 and 7, the wavelength of the light is measured to a precision of ten significant digits using a wavelength meter (WLM) coupled into the data acquisition. The wavelength of the laser should match the transitions of the two-photon process described in Section 2.2.2, which is at $\lambda \approx 860$ nm. The output beam coming from a launcher is split into two paths, E and F, using a beam splitter to ensure that the light remains in phase. Using collimating lenses with a 15 cm focal length, each resulting beam is directed through an AOM. The AOMs in paths E and F have commercially available design frequencies of 80 ± 20 MHz and 200 ± 40 MHz, respectively [28]. Their operating frequencies are 100 MHz and 165 MHz. For consistency with prior documentation, the AOMs are labeled "AOM100" and "AOM165" using a suffix notation denoting their frequencies. The main beam is blocked directly after the AOMs, so

only the first order diffracted beams with a frequency difference matching the hyperfine splitting of the BaF spin states continue in the setup. The net two-AOM system diffraction efficiency can be evaluated based on the weighted efficiency (WE) of

$$WE = \frac{P_{100} \cdot \eta_{100} + P_{165} \cdot \eta_{165}}{P_{100} + P_{165}}, \tag{23}$$

where P_{100} and P_{165} are the powers incident on the AOM100 and AOM165, respectively, and η_{100} and η_{165} are the corresponding diffraction efficiencies. The AOMs require an amplifier to function. The amplified signal goes into an RF switch and RF pulses generated by function generators (RIGOL DG4162, DG4202) are employed for the timing of the two-pulse sequence: if the AOM does not get any RF power, there is no laser power going into the sidebands, and thus no light going to the experiment. This allows for advanced temporal control over the applied laser pulses. The first order diffracted beams continue to go through lenses with a 10 cm focal length, whereafter they are aligned into optical fibers E and F, respectively, using mirrors. These optical fibres send the beams towards the second part of the optical configuration after they are led through FiberControl FPC-3 devices for polarization control [20].

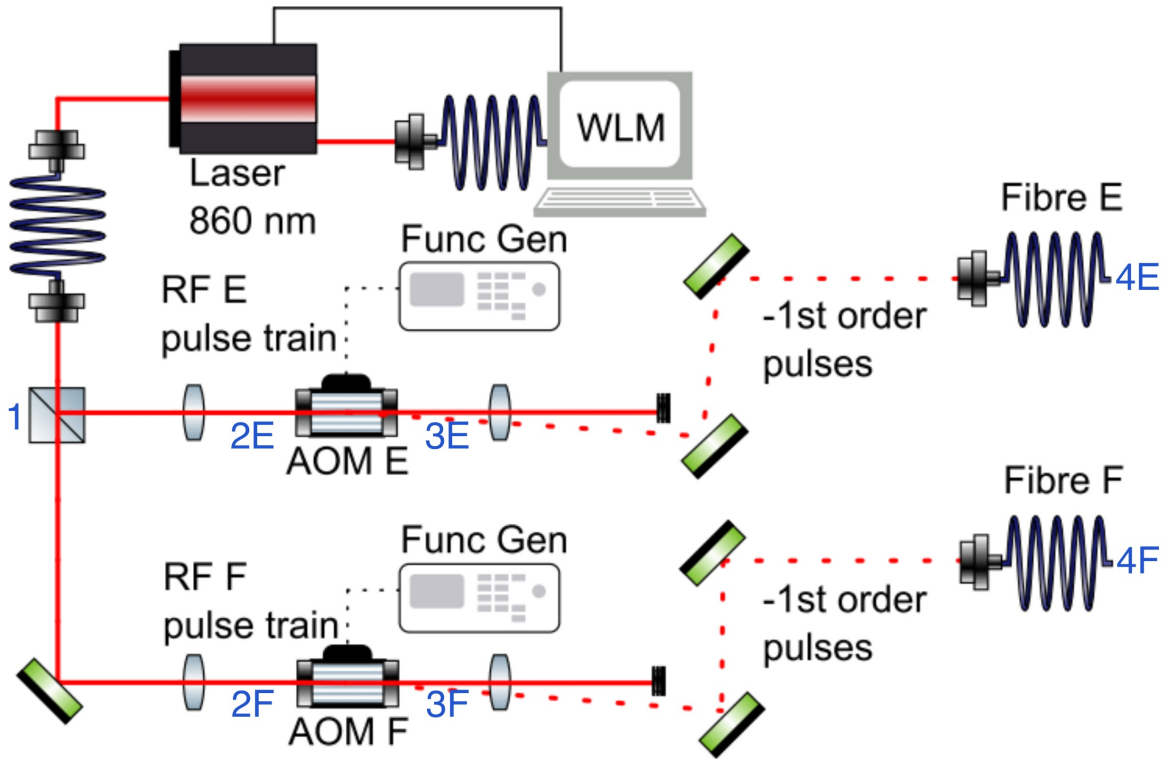

Figure 6: Schematic of the first part of the optical configuration. The $\sim$ 860 nm output beam from a diode laser is split into two paths, E and F, using a beam splitter to ensure phase coherence. Each beam is collimated and passes through an acousto-optic modulator (AOM), driven by independently timed RF pulses generated at 100 MHz and 165 MHz. The first-order diffracted beams, with a frequency difference matching the hyperfine splitting of the BaF spin states, are aligned into optical fibers for delivery to the second part of the optical chain. The blue labels (1 – 4E/F) indicate key diagnostic stages. Not shown are the FPC-3 polarization control units used to maximize the passthrough power that interacts with the molecules. Figure adapted from [20].

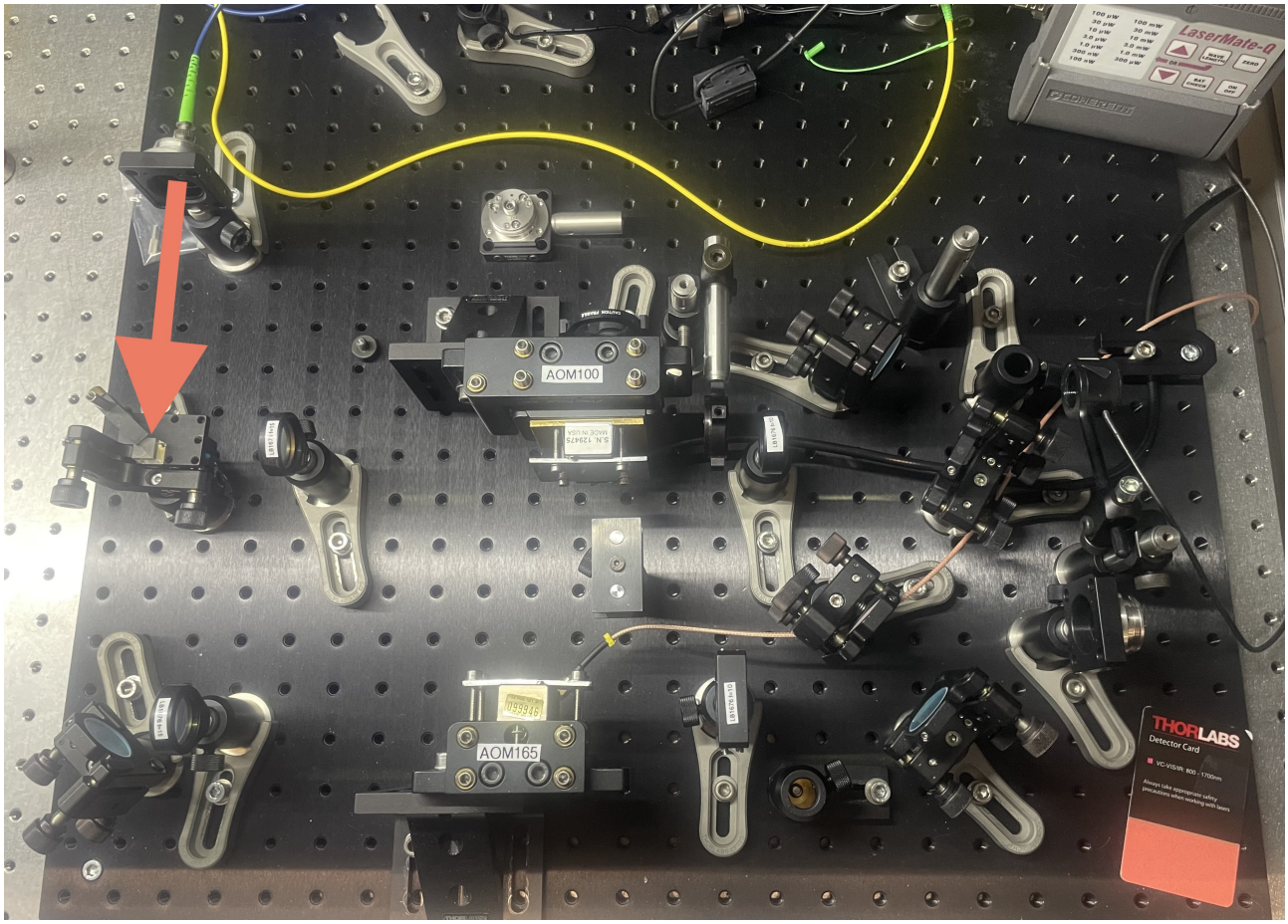

Figure 7: Photograph of the first part of the optical configuration on a laboratory optical table. The arrow indicates the initial direction of the output laser beam. This setup corresponds to the schematic shown in figure 6.

In the second part of the optical configuration, shown in figures 8 and 9, the opposite polarization components of the outputs of fibres E and F are recombined using a polarising beam splitter. Polarisation control is adjusted to maximize the optical power transmitted as passthrough power to the molecular beam. To ensure that no phase difference is created between beams E and F, their distance traveled by the light before going into the PBS has to be equal. The combined beam is expanded to a radius of 20(2) mm by a telescope [17] and aligned to interact with the molecular beam. A variable aperture is used to block all but the central portion of the expanded beam, effectively isolating the most uniform and intense region.

To monitor beam alignment, several components are added to the second part of the configuration. As a first check for overlap, the two other oppositely polarised beams from the PBS, which do not go to the molecular beam, are routed through an optical fibre into a fibre-coupled FGA04 InGaAs IR photodiode. Successfully coupling both beams into the same fibre requires a reasonable degree of spatial and angular overlap as fibre coupling is highly sensitive to beam alignment. The photodiode also measures the power in these polarization components, which is referred to as the split-off power. Minimizing the split-off power maximizes the power in the counterpropagating beams that will interact with the molecular beam. Additionally, two wedge beam splitters divert a portion of the passthrough power onto a Thorlabs camera, providing a quantitative check of the spatial overlap based

on spot size. The first wedge is placed right after the PBS and the second right before the beam expander, ensuring a maximum difference in traveled distance to identify potential small misalignment. Complete overlap is confirmed if the spot sizes measured at the two points are equal to each other. A third wedge beam splitter sends part of the combined passthrough beam through a second PBS onto two Thorlabs DET36A/M Si detectors in order to measure the powers of the individual polarization components.

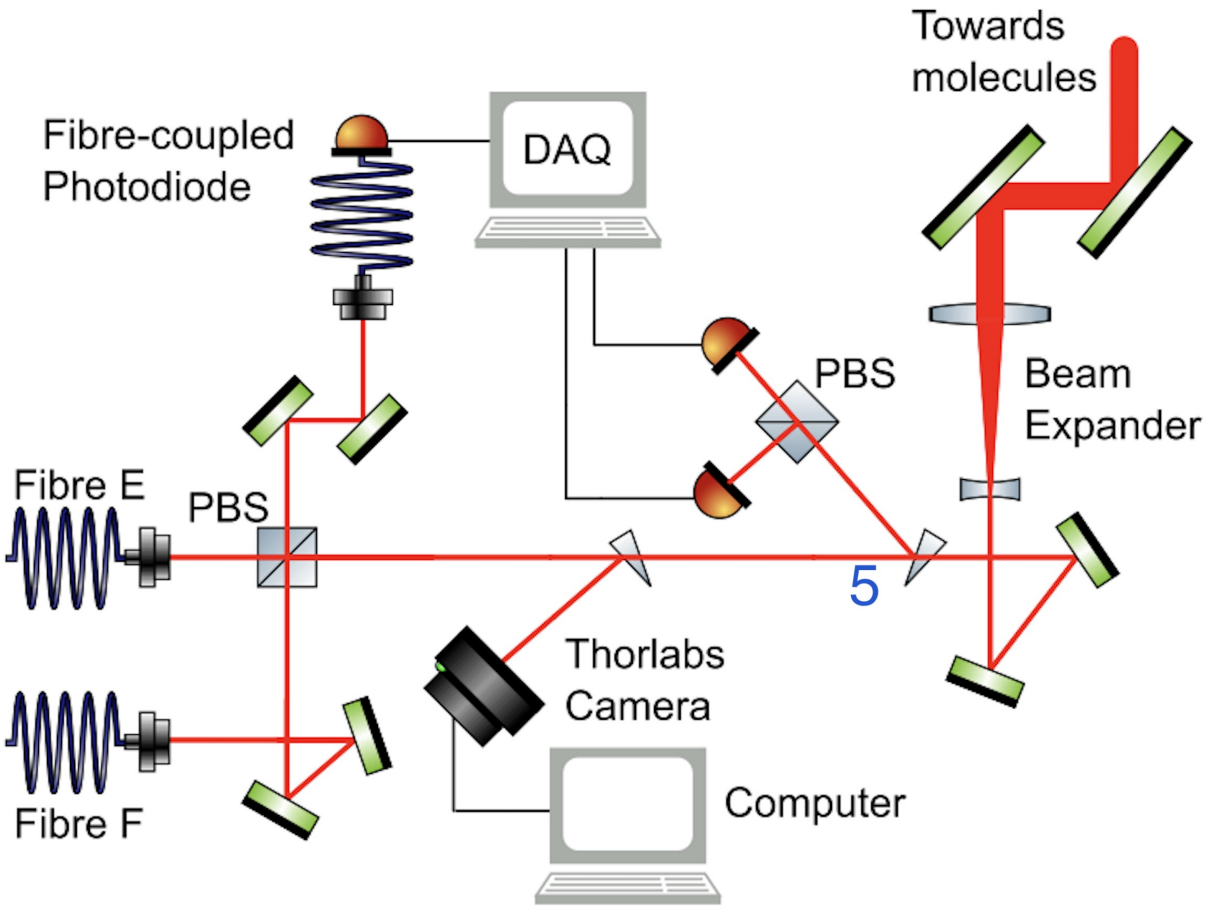

Figure 8: Schematic overview of the second part of the optical configuration. The outputs of fibers E and F are recombined using a polarizing beam splitter (PBS), with optical path lengths carefully matched to avoid phase drift. The combined beam is expanded using a telescope and spatially filtered using a variable aperture to isolate the uniform central region of the Gaussian intensity profile. Several diagnostic tools assist with beam alignment. A fiber-coupled photodiode monitors orthogonally polarized light split off by the PBS, providing an initial check for spatial and angular overlap and allowing power measurements of the individual polarization components. Two wedge beam splitters, one of which is not shown, divert portions of the passthrough beam to a Thorlabs camera for spot size comparison at different locations, serving as a diagnostic for beam divergence. A third wedge splitter samples the combined passthrough beam for power measurements of its individual polarization components. The blue label (5) indicates the diagnostic stage for passthrough power measurements. Figure adapted from [20].

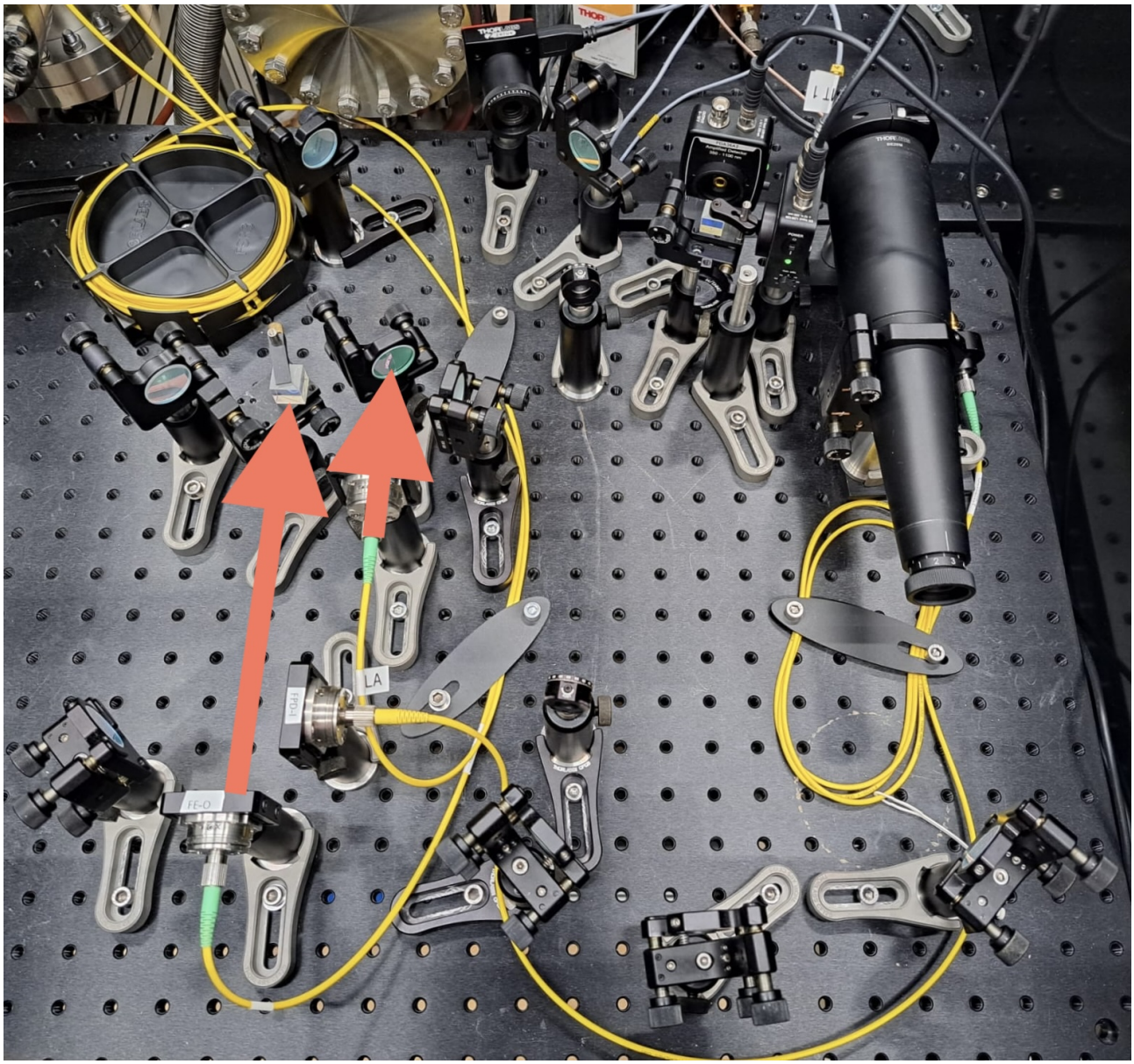

Figure 9: Photograph of the second part of the optical configuration near the interaction zone. The arrows indicate the initial directions of the two beams, E and F, exiting the optical fibers. This setup corresponds to the schematic shown in figure 8.

4 Power Losses in the Optical Configuration

This section presents the results and interpretation of the experimental characterization of power losses in the counterpropagating laser system. Power transmission is quantified at key points along the optical path to assess the performance and reliability of the configuration. The performance of the acousto-optic modulators (AOMs) is extensively analyzed to identify potential strategies for improving diffraction efficiency and maximizing overall power transmission.

4.1 Overview of Optical Power Transmission

Optimization of the counterpropagating laser involves minimizing power losses throughout the entire optical chain: from the laser source, through AOMs and fiber couplers, to the final interaction region. Using a Coherent LaserMate-Q Power Meter, the laser power was measured at several stages of the optical configuration to a precision of 0.01 mW. Table 1 provides an overview of the power losses at different stages in the optical chain as depicted in figure 6.

Position in optical chain	**Sequential power loss (%)**	**Total power loss (%)**
1	0	0
2E	8 ± 3	8 ± 3
2F	10 ± 3	10 ± 3
3E	65.1 ± 0.9 at 1500 mW*	67.9 ± 0.3 at 1500 mW*
3F	58 ± 2 at 1000 mW*	62.1 ± 0.3 at 1000 mW*
4E	31.7 ± 0.9	78.1 ± 0.4
4F	21 ± 2	70.1 ± 0.8

Table 1: Power losses of the counterpropagating laser beams at different stages in the optical chain. The second column lists sequential losses relative to the previous stage, while the third column lists total losses relative to the initial beam power. Since the output beam is split into two paths, the total losses are expressed with respect to half of the output power of the laser. *The power loss is equal to 100% minus the AOM diffraction efficiency, which is plotted for increasing acoustic voltages in figures 10 and 11.

4.2 Diffraction Efficiency and Insertion Losses

One primary source of power loss arises from intended diffraction by the AOMs, which only diffract a fraction of the input laser power into the first-order beam. To quantify the diffraction efficiency, the power in the first-order diffracted beam (P_1) is measured as a function of RF drive power, in accordance with equation 19. Figures 10 and 11 confirm that increasing RF voltage improves diffraction efficiency up to a saturation point. However, even without applied RF power, insertion losses occur due to imperfect anti-reflection coatings and absorption in the crystal, as described by equation 22. These losses are $23 \pm 3\%$ for the AOM100 and $12 \pm 4\%$ for the AOM165. Both values are substantial and may result from mismatches between the materials in the AOMs and the optical wavelength of the counterpropagating laser, which is measured to be 859.63757 ± 0.00001 nm by the wavelength meter. Another contribution to the $11 \pm 5\%$ difference in insertion losses may be a difference in active aperture size. A smaller active aperture of the AOM offers less tolerance for beam alignment, increasing the likelihood of clipping at the crystal boundaries.

The difference in insertion losses propagates to a difference in saturation values of the diffraction efficiencies. Since diffraction efficiency is defined as a ratio of diffracted to incident power, higher insertion losses naturally limit achievable efficiency. For the AOM100, the curve begins to saturate at approximately 1500 mV around 35%, as seen in figure 10. For the AOM165, the curve begins to saturate at approximately 1000 mV around 45%, as seen in figure 11. When maximum diffraction efficiency is reached, applying additional RF power offers no further improvement. Given that AOMs operating in the Bragg regime typically do not exceed a 50% efficiency for moderate acoustic powers [26], these results are not anomalous, although there is some room for improvement. Enhancement can still be realised by optimizing the beam waist position to lie at the center of the AOM crystal, as well as by fine-tuning the acoustic drive frequencies.

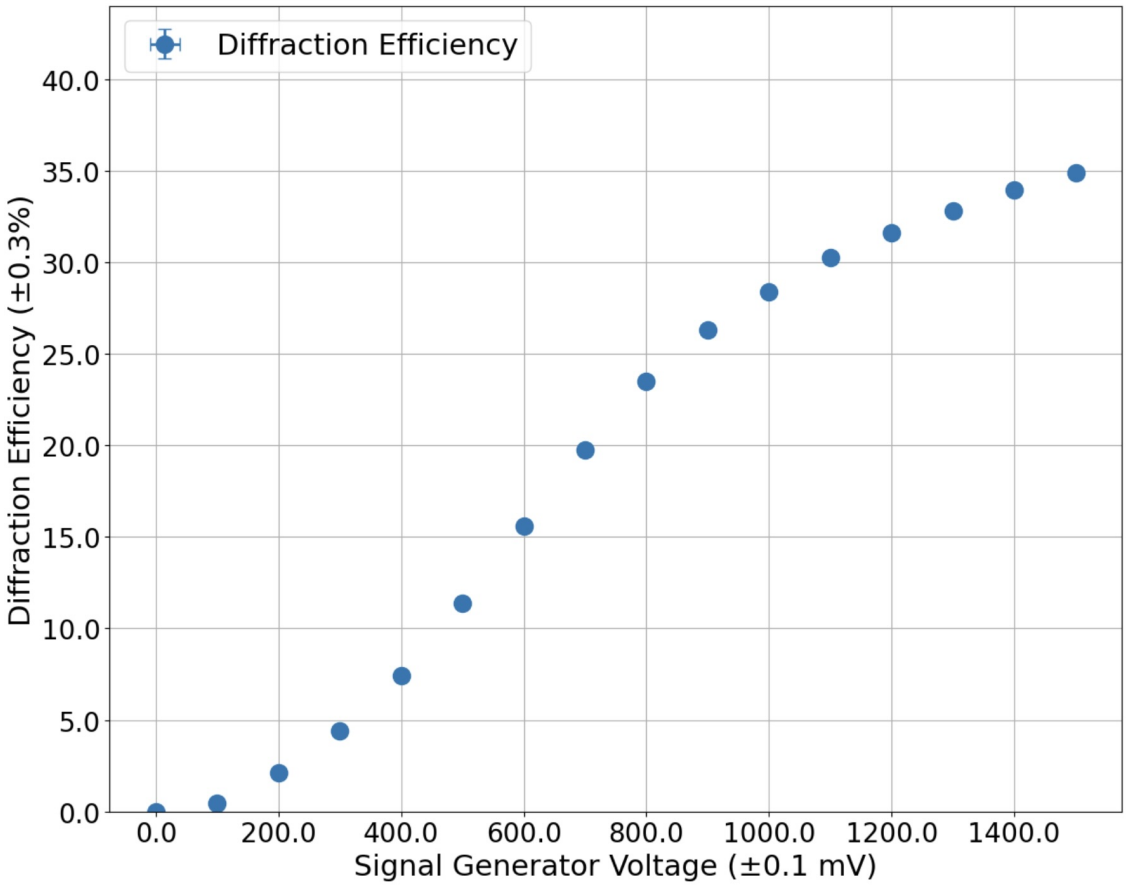

Figure 10: Diffraction efficiency of the AOM100 as a function of the signal generator voltage applied to the AOM crystal. Note that the measurement uncertainty is smaller than the symbol size.

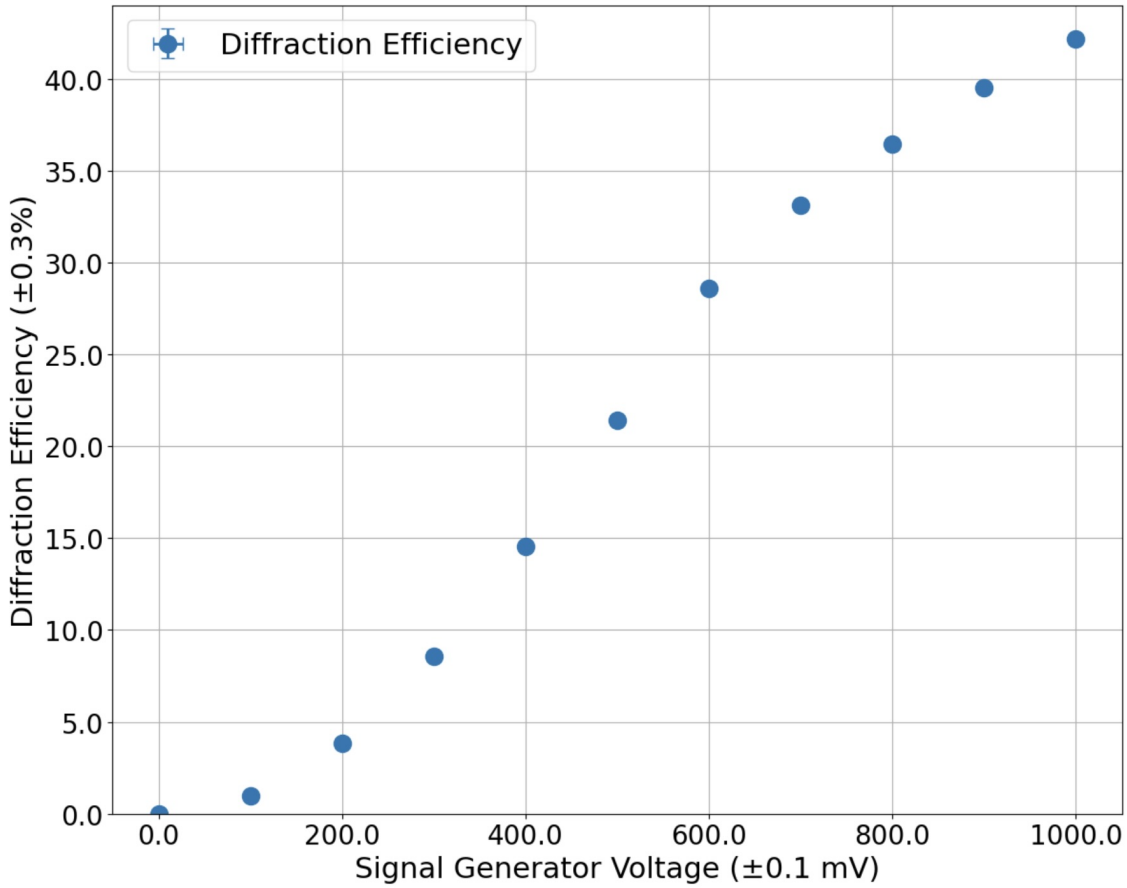

Figure 11: Diffraction efficiency of the AOM165 as a function of the signal generator voltage applied to the AOM crystal. Note that the measurement uncertainty is smaller than the symbol size.

4.3 Optimization of AOM Performance

To minimize power losses in the optical chain, the diffraction efficiencies of the AOMs must be optimized. This involves precise alignment to ensure that the collimating lenses focus the incident Gaussian beams properly onto the AOM crystals. In addition, the AOMs should operate at appropriate acoustic frequencies, satisfying the Bragg condition. This section examines whether adjustments to beam waist positioning and drive frequencies can improve diffraction efficiencies and thereby enhance overall system performance.

4.3.1 Beam Waist Positioning

The lenses used to focus the incident beams onto the AOM crystals have a focal length of $f = 15.0 \pm 0.3$ cm, assuming a 2% manufacturer tolerance. At the position of these lenses, the beam diameter is estimated to be $d_l = 1.5 \pm 0.1$ mm. Applying equations 14 and 15, this yields a beam waist of $W_0 = 55 \pm 4\,\mu$m and a corresponding spot size of $d_0 = 110 \pm 8\,\mu$m. The Rayleigh range z_0, as defined by equation 17, is $z_0 = 11 \pm 2$ mm, giving a depth-of-focus of $DOF = 22 \pm 4$ mm according to equation 18.

Under the assumptions outlined in section 3.2, the beam waist is located precisely at the focal point at $z = 15.0 \pm 0.3$ cm along the optical axis. The center of the AOM crystal is measured to lie at $z = 14.5 \pm 0.1$ cm, which is well within the Rayleigh range. Figure 12 shows the beam radius as a function of distance z from the collimating lens based on equation 16. At the center of the crystal, the beam radius is $W(14.5\text{ cm}) = 60 \pm 8\,\mu$m, which is 1.1 ± 0.2 times than the beam waist. This negligible difference indicates a tightly focused beam at the point of interaction, enabling efficient acousto-optic modulation. Consequently, neither the diffraction efficiencies nor the bandwidths benefit significantly from further focusing adjustments.

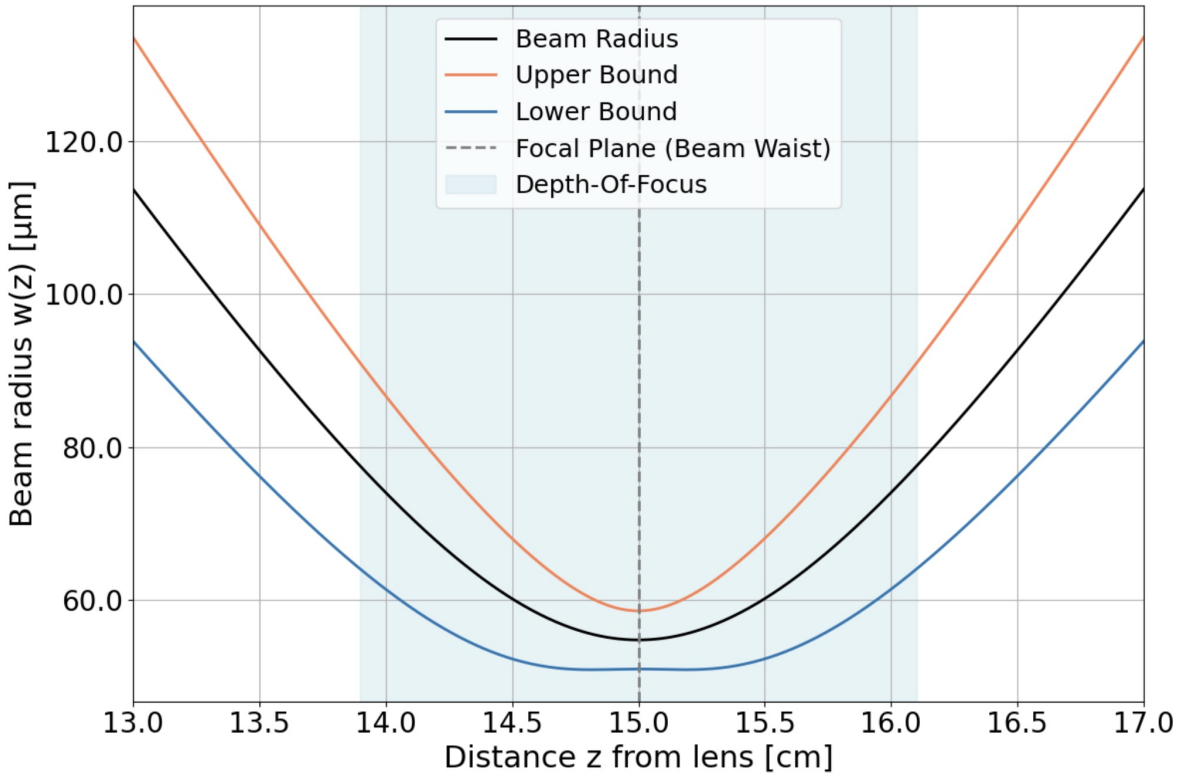

Figure 12: Calculated Gaussian beam radius $W(z)$ as a function of distance z along the optical axis, measured from a collimating lens with a focal length of 15 cm. The central curve represents the nominal beam radius, while the upper and lower bounds reflect the uncertainties in beam waist W_0 and Rayleigh range z_R. The beam waist is assumed to be located precisely at the focal point of the collimating lens. The depth-of-focus is the region within which the beam radius increases by a factor of $\sqrt{2}$ relative to the beam waist.

4.3.2 Operating Acoustic Frequencies

Another factor that influences the diffraction efficiency is the acoustic drive frequency. Although the AOMs are designed for 80 and 200 MHz, they are operated at 100 and 165.875 MHz, respectively. Figures 13 and 14 show the diffraction efficiencies of the AOMs for different operating acoustic frequencies. The considered frequency ranges are constrained by the requirement to match the frequency difference to the hyperfine splitting of the BaF spin states. The weighted diffraction efficiencies of valid AOM frequency pairs, obtained by applying equation 23, are listed in table 2.

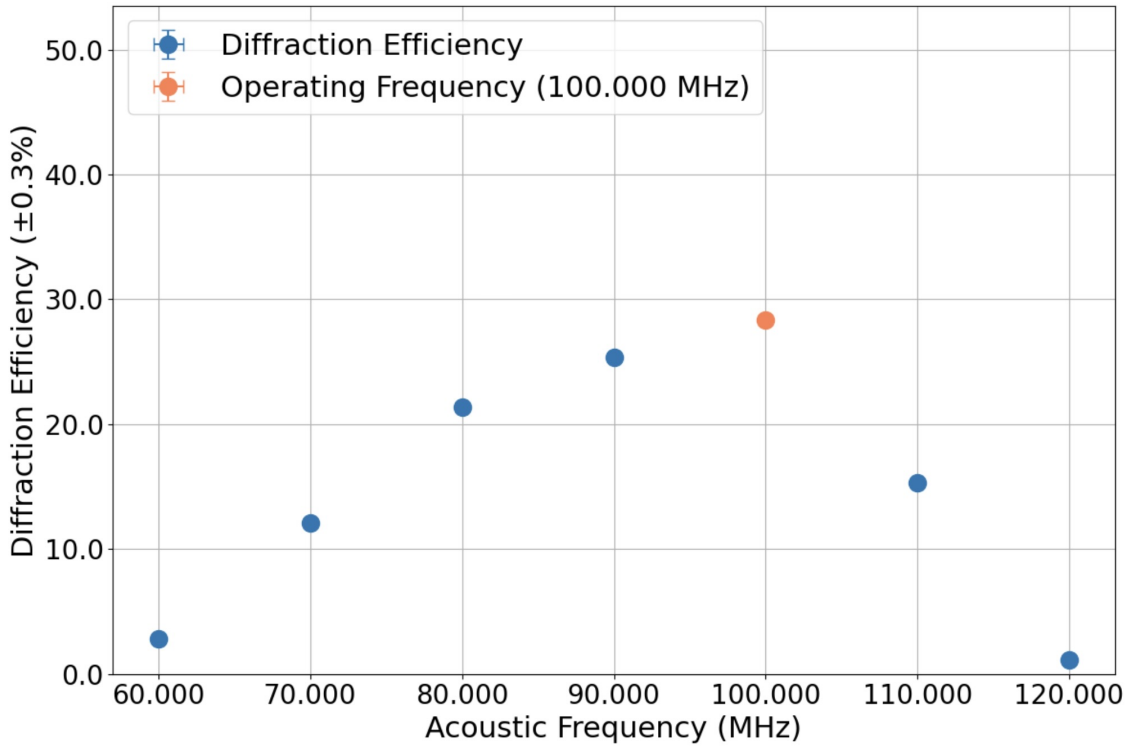

Figure 13: AOM100 diffraction efficiency as a function of acoustic drive frequency at a signal generator voltage of 1000 mV. Note that the measurement uncertainty is smaller than the symbol size.

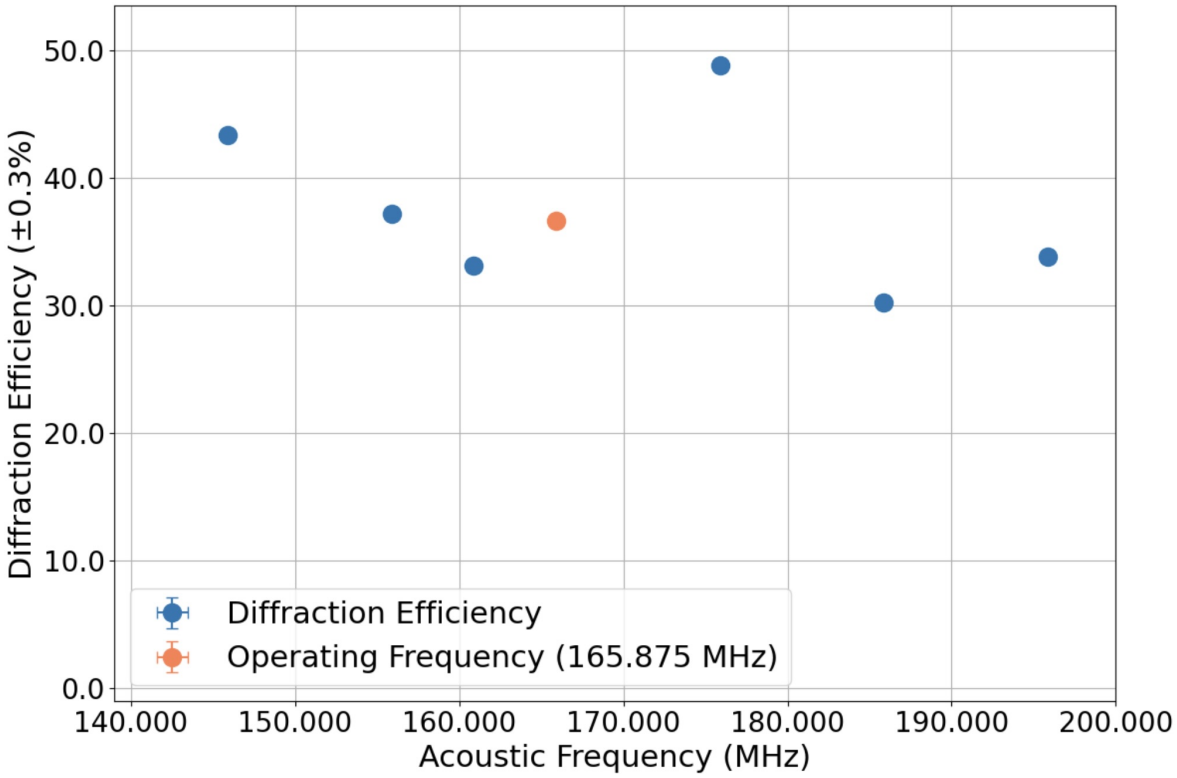

Figure 14: AOM165 diffraction efficiency as a function of acoustic drive frequency at a signal generator voltage of 800 mV. Note that the measurement uncertainty is smaller than the symbol size.

AOM100 acoustic frequency ($\pm$0.001 MHz)	AOM165 acoustic frequency ($\pm$0.001 MHz)	Weighted diffraction efficiency (%)
80.000	145.875	32.2 ± 0.6
90.000	155.875	31.1 ± 0.6
100.000	165.875	32.5 ± 0.6
110.000	175.875	31.9 ± 0.7
120.000	185.875	15.5 ± 0.4

Table 2: Weighted diffraction efficiency of the two-AOM system for various valid combinations of operating acoustic frequencies.

The currently selected frequencies form an efficient combination, yielding a weighted diffraction efficiency of $32.5 \pm 0.6\%$ at signal generator voltages of 1000 mW for the AOM100 and 800 mW for the AOM165. Operating the AOMs closer to their saturation voltages can still increase the listed diffraction efficiencies. Notably, it is possible to operate the AOMs over a wider range of frequencies, since the system efficiency shows negligible differences between several frequency combinations. Even though the AOMs perform effectively at their operating frequencies, some deviations from ideal behavior are observed in the diffraction efficiency as a function of acoustic frequency. Typical AOM behaviour would show a bell-shaped curve around the design frequency ranging from zero to the saturation diffraction efficiency [29]. The AOM100 displays this expected bell-shaped response, though with a maximum diffraction efficiency at 100 MHz rather than at its design frequency of 80 MHz. The AOM165, however, shows oscillatory behavior with diffraction efficiencies between $\sim$ 30-50% and a maximum at 175.875 MHz rather than at its design frequency of 200 MHz. This oscillatory behavior potentially indicates acoustic reflections within the AOM crystal. If this is the case, standing waves are formed which interact with the forward-propagating acoustic wave, resulting in interference in the acoustic drive amplitude. Because the position of the constructive versus destructive interference varies with frequency, this leads to frequency-dependent modulation of the acoustic field strength. These effects are typically due to internal factors such as impedance mismatches between the crystal and the transducer. However, the irregular behavior does not necessitate immediate action, since the AOMs still perform effectively at the selected operating frequencies.

4.4 Fiber Coupling and Total Power Transmission

In addition to AOM-related losses, fiber coupling is another main source of power loss as seen in table 1. Subsequent to the frequency modulation, the first-order diffracted beams are transmitted via optical fibers to the second part of the configuration. To maximize coupling efficiencies, the beams are carefully aligned into the fibers using mirrors, whereafter polarization is optimized. The resulting efficiencies are $68.3 \pm 0.9\%$ for path E and $79 \pm 2\%$ for path F. This is consistent with typical fiber coupling performance, which can go up to 80% [30].

The cumulative result of all sequential losses is that $21.9 \pm 0.4\%$ and $29.9 \pm 0.8\%$ of the initial laser power in paths E and F, respectively, reaches the second part of the optical chain. Although suboptimal, these transmission levels are sufficient for creating high-intensity counterpropagating beams for molecular interaction. Reducing power losses further could improve laser resource efficiency and the signal-to-noise ratio. However, the current configuration meets the experimental requirements.

4.5 Conclusion

Systematic measurements quantified the optical power losses across the counterpropagating laser configuration, showing that $21.9 \pm 0.4\%$ and $29.9 \pm 0.8\%$ of the initial laser power in paths E and F, respectively, reaches the second part of the optical chain. These losses originate primarily from intended diffraction, AOM insertion losses, and imperfect fiber coupling. The fiber coupling efficiencies were measured to be $68.3 \pm 0.9\%$ for path E and $79 \pm 2\%$ for path F, consistent with typical performance reaching up to 80%. The insertion losses of $23 \pm 3\%$ for the AOM100 and $12 \pm 4\%$ for the AOM165 propagate to saturation diffraction efficiencies of around 35% and 45%, respectively. These values are not anomalous for practical implementations, though some room for improvement remains. Optimization efforts confirmed that the Gaussian beam waists are well aligned with the AOM crystals, enabling efficient acousto-optic interaction. The selected acoustic drive frequencies of 100 MHz and 165 MHz also proved effective. Notably, the AOMs can be operated over a broader range of frequencies without significantly impacting the diffraction efficiencies, which offers useful flexibility for tuning or future adjustments. Further optimization of AOM parameters shows no significant potential for gains in transmission. However, such improvements are also not deemed necessary, as the current optical configuration delivers counterpropagating beams with sufficient power for high-intensity interaction with the molecules.

5 Power Stability

This section analyzes the temporal stability of the optical power in the second part of the configuration. Three quantities are examined: the passthrough power, which reaches the molecular beam; the split-off power, which is diverted by the polarizing beam splitter and does not interact with the molecules; and the total power, which is defined as the sum of the passthrough and split-off powers. Among these, the passthrough power is most critical, as it directly governs the coherence of the quantum state transfer. Ideally, the total power should remain stable as well, regardless of polarization control.

5.1 Passthrough Power

The stability of the passthrough power was monitored over several days by feeding it into the data acquisition system at stage 5 of the optical configuration, as depicted in figure 8. For safety reasons, only the laser beam in path E was operated at moderate power during the measurement period, while the laser beam in path F remained blocked. The results, presented in figure 15, indicate an average passthrough power of $P_0 = 0.945 \pm 0.005$ mW. The maximum recorded value, $P_{max} = 0.980 \pm 0.005$ mW, corresponds to a $3.7 \pm 0.8\%$ increase relative to the average. The minimum recorded value, $P_{min} = 0.890 \pm 0.005$ mW, corresponds to a $5.8 \pm 0.8\%$ decrease.

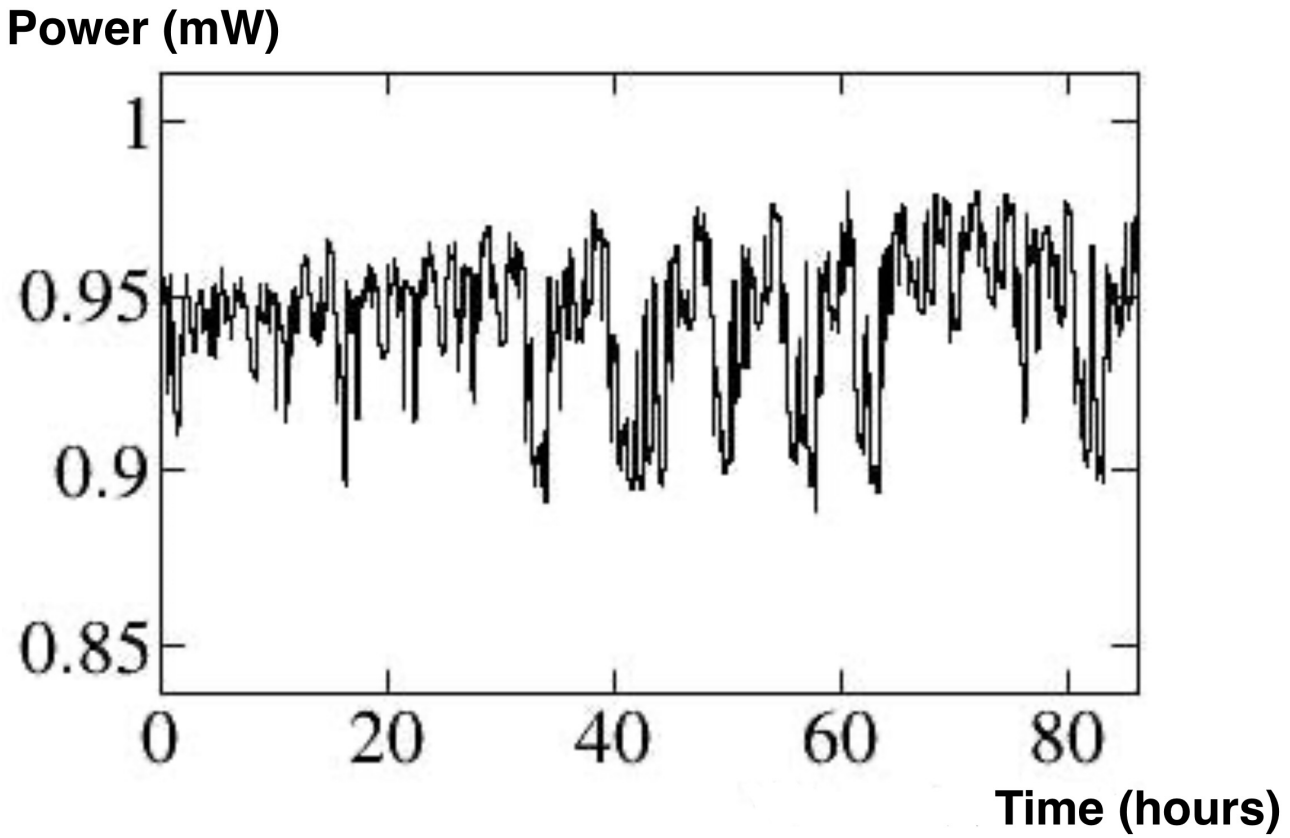

Figure 15: Measured stability of the passthrough power, defined as the portion of the laser beams transmitted by the polarizing beam splitter toward the molecular beam, over several days of operation. Only the laser in path E was active and operated at moderate power for safety.

Fluctuations in passthrough power directly influence the two-photon Rabi frequency Ω_{EF} as described by equations 10 and 11. Assuming that the laser beam in path F behaves similarly to the beam in path E, a model was developed to quantify the impact. The corresponding Python code, shown in appendix A, generates figure 16. The worst-case combination of $\frac{P_E}{P_{E,0}} = 0.942$ and $\frac{P_F}{P_{F,0}} = 1.037$, which are the minimum and maximum observed passthrough power ratios, yields a normalized two-photon Rabi frequency of $\frac{\Omega_{EF}}{\Omega_{EF,0}} = 0.988 \pm 0.006$. This corresponds to a maximum reduction of $1.2 \pm 0.6\%$ in Ω_{EF} and a proportional decrease in Rabi phase ϕ_R, which is accumulated during the 50 μs laser pulses. While such deviations could in principle reduce the fidelity of quantum state transfers, it is important to consider the timescale over which these measurements were conducted. The relevant timescale for reliable eEDM extraction is on the order of 10 seconds, which is the duration of individual measurement cycles over electric field reversal. As such, the observed long-term power fluctuations are unlikely to significantly impact the coherence of the quantum state transfer. However, because the experiment must run continuously for months to collect sufficient statistics, the observed fluctuations can still affect the overall data quality. A practical solution is to monitor the passthrough power continuously throughout the measurement, allowing the fluctuations to be corrected during data analysis.

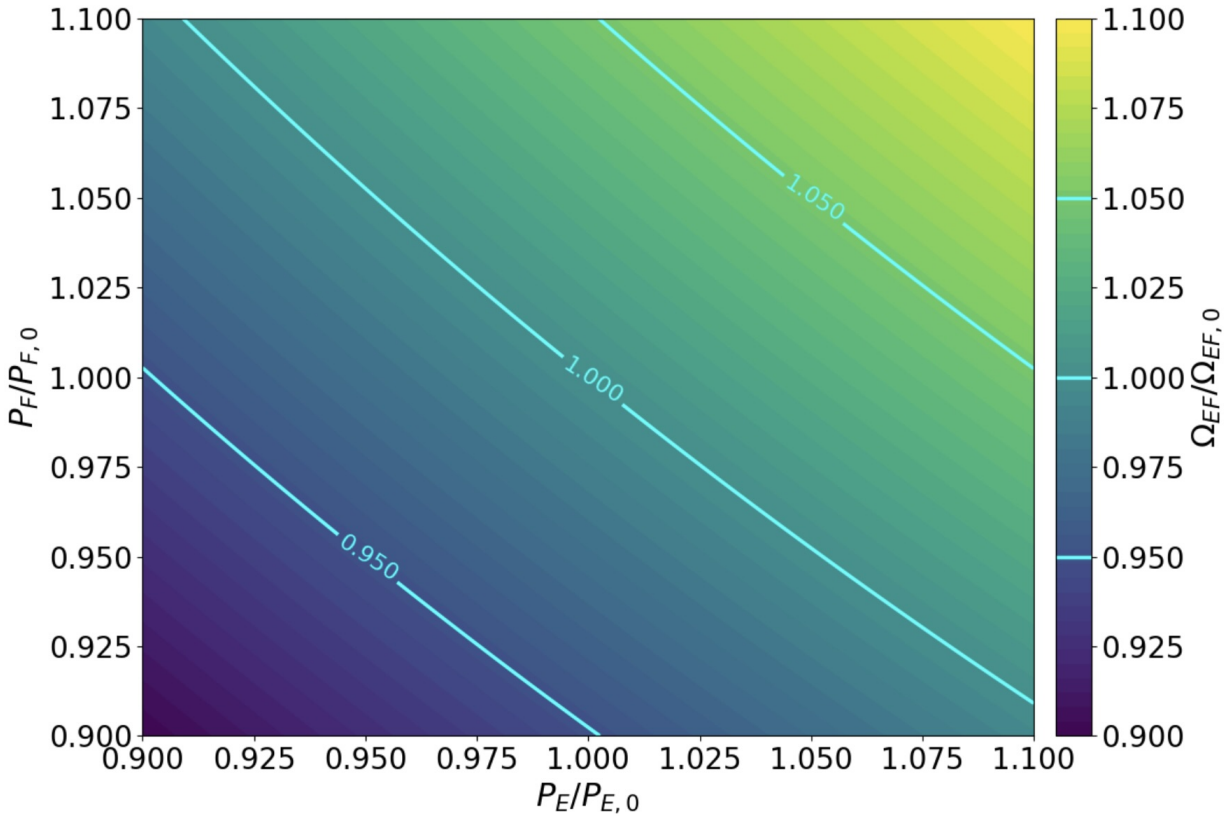

Figure 16: Modeled dependence of the normalized two-photon Rabi frequency $\frac{\Omega_{EF}}{\Omega_{EF,0}}$ on independent fluctuations in the passthrough power ratios $\frac{P_E}{P_{E,0}}$ and $\frac{P_F}{P_{F,0}}$ for the beams in paths E and F. Each point in the heatmap represents a specific combination of power ratios, with contour lines indicating constant values of the normalized Rabi frequency. For example, if the powers in paths E and F are at their average values, the intersection near the coordinates of $\frac{P_E}{P_{E,0}} = 1$ and $\frac{P_F}{P_{F,0}} = 1$ yields a normalized Rabi frequency of $\frac{\Omega_{EF}}{\Omega_{EF,0}} = 1$, corresponding to the ideal case. This visualization illustrates how realistic power drifts in either beam affect the two-photon Rabi frequency, providing a quantitative measure of the sensitivity of the system to such fluctuations.

5.2 Total Power

The stability of both the split-off and total power was monitored over several days, in parallel with the passthrough power. Figure 17 shows an average split-off power of $P_{so} = 0.0035 \pm 0.0005$ mW, with occasional bursts up to approximately 0.01 mW. The absolute magnitude of these fluctuations is smaller than those observed in the passthrough power. Consequently, the total power is not constant, as shown in figure 18. The average total power is $P_{tot} = 0.95 \pm 0.01$ mW, meaning that fluctuations of approximately 1% are observed relative to the average. These minor variations are likely caused by mechanical vibrations and occasional mode hopping in the laser, leading to drifts over the measurement period.

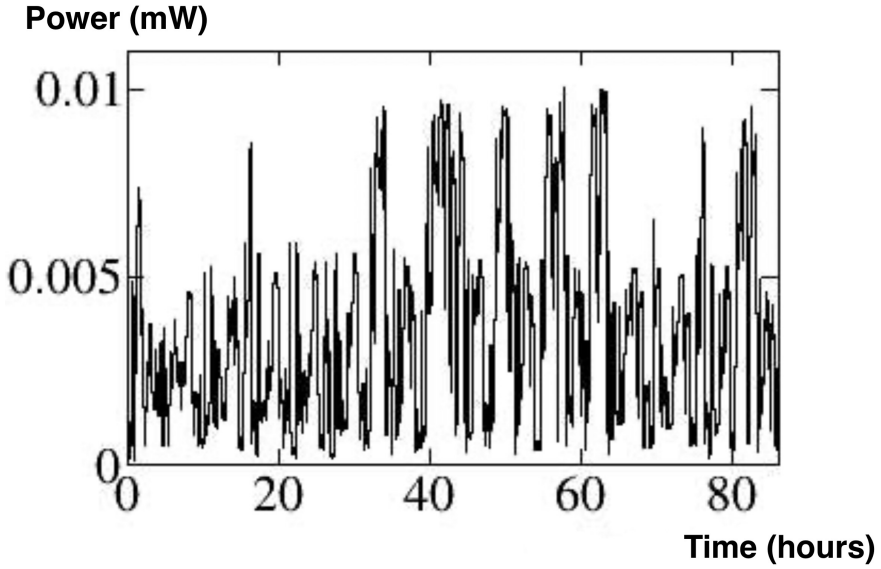

Figure 17: Measured stability of the power split off by the polarizing beam splitter, recorded under the same experimental conditions as the passthrough power.

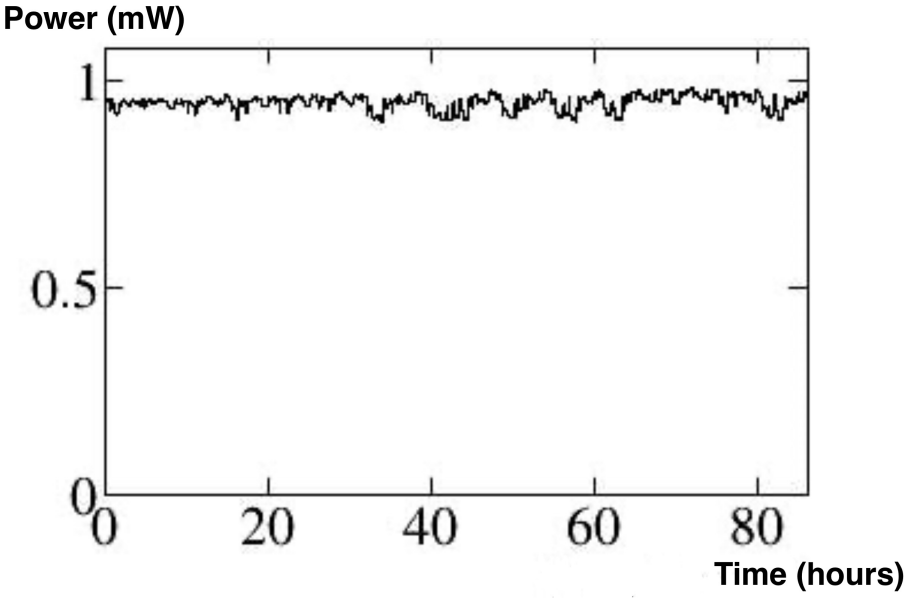

Figure 18: Measured stability of the total power, defined as the sum of the passthrough power and split-off power, in the second part of the optical configuration.

5.3 Conclusion

The power stability measurements presented in this section reveal that the optical output of the counterpropagating laser system exhibits minor fluctuations over the course of several days. Total power variations remain within approximately 1% relative to the average and are likely caused by mechanical vibrations or mode hopping in the laser. More critical is the stability of the passthrough power, which directly affects the two-photon Rabi frequency Ω_{EF}. Observed passthrough fluctuations range from $+3.7 \pm 0.8\%$ to $-5.8 \pm 0.8\%$ relative to the average, resulting is a worst-case reduction of $1.2 \pm 0.6\%$ in Ω_{EF}. On the relevant timescale of individual measurement cycles, which about 10 seconds, these fluctuations are unlikely to significantly degrade the fidelity of the quantum state transfer. However, the experiment must be operated continuously for months to gather sufficiency statistics, so the observed fluctuations will affect the overall data quality. A practical solution is continuous monitoring of the passthrough power, enabling corrections during data analysis to preserve the accuracy of the eEDM result.

6 Summary, Limitations and Outlook

6.1 Summary of Main Contributions

This thesis set out to characterize and optimize the counterpropagating laser system used in the NL-eEDM experiment, with a focus on the delivery and stability of the optical power required for high-fidelity quantum state manipulation of BaF molecules. By minimizing power losses, optimizing acousto-optic modulator (AOM) performance, and monitoring laser power stability, this work supports the broader experimental effort to enhance sensitivity to a permanent electron electric dipole moment (eEDM) in the search for Beyond the Standard Model (BSM) physics. Systematic measurements quantified optical power losses throughout the configuration, identifying intended diffraction, AOM insertion losses, and imperfect fiber coupling as the main contributors. The AOMs were confirmed to be well-aligned with the Gaussian beam profile and operated at efficient acoustic frequencies. No anomalous power losses were observed, and the system delivers sufficient power for high-intensity interaction with the molecular beam. Power stability measurements over multi-day timescales revealed small intensity fluctuations in the passthrough beams that are sent to interact with the molecules. While these variations are unlikely to affect coherence within individual measurement cycles, they do impact long-term statistical data collection. Continuous monitoring of the passthrough power is therefore recommended to enable correction during data analysis. In conclusion, the counterpropagating laser system meets its operational requirements and is ready to be used in future eEDM measurements.

6.2 Limitations and Outlook

While the optical configuration is analyzed comprehensively, some limitations remain. A primary limitation lies in the lack of access to the exact specifications of the AOMs used in the optical chain. The AOMs were already mounted within their alignment casings, preventing direct verification of their product types or technical datasheets. Efforts to retrieve this information through administrative records have not been successful. As a result, explanations for the observed insertion loss differences, such as suboptimal anti-reflection coatings or a difference in active aperture size, remain speculative. While dismounting the AOMs could provide clarity, this would require realigning the entire optical chain, which is unnecessary given that current AOM performance meets typical standards.

A second limitation is that all power stability measurements were performed using only the beam in path E, operated at moderate power. The optical beam in path F was blocked during these measurements. It was assumed that power fluctuations in this path are similar to those in path E, but this lacks empirical verification. As such, the model used to relate power fluctuations to the two-photon Rabi frequency is based on a partial dataset. Simultaneous monitoring of both beams under typical operating conditions would improve the accuracy and reliability of the stability analysis. Moreover, expanding the current model to include the effect on the final molecular populations at the readout stage would provide a more complete picture of how deviations from ideal π-pulses affect experimental observables. Potential systematic shifts introduced by power fluctuations could then be mitigated by adjusting the pulse duration accordingly or by incorporating appropriate corrections into the data analysis. In addition, a more detailed assessment on shorter timescales would be beneficial, as the passthrough power is specifically required to remain stable throughout individual measurement cycles over electric field reversal.

Another limitation arises from the sensitivity of the fiber coupling process, which proves highly vulnerable to small misalignments. While high coupling efficiency could be achieved initially, it was occasionally observed to drop without a clear cause, requiring realignment. Additionally, mechanical stress or bending of the optical fibers alters the polarization state of the transmitted beams. Since the passthrough power is transmitted by a polarizing beam splitter, such changes can lead to reduced power delivered to the molecular beam. Improved mechanical stabilization of the fiber positions could enhance power stability compared to the current configuration.

Despite its limitations, this thesis provides a detailed and quantitative characterization of the counterpropagating laser system in the NL-eEDM experiment. The analysis forms a solid foundation for evaluating the reliability of the experimental parameters within the optical configuration.

Acknowledgments

I would like to thank Lorenz Willmann for giving me the opportunity to work on a thesis project so closely aligned with my interests. You have been very helpful and supportive throughout the process: from offering me a lab tour when I first expressed interest, to providing lots of feedback throughout the project. I am also grateful to Jelmer Levenga for his daily guidance in the lab. You made me feel welcome from the start and taught me a great deal of practical skills. Your willingness to answer questions and provide feedback at every step has been very valuable, and I truly appreciate your patience and encouragement. Lastly, I would like to thank the entire NL-eEDM collaboration for welcoming me into the daily operation of the experiment. I genuinely felt part of the team. Being involved in such a large and well-organized collaboration has been a valuable experience and has made me realize that I want to pursue this path further in my academic career.

Bibliography

[1] T. Meijknecht, *Electric and Magnetic Field Control for Electric Dipole Moment Searches*. PhD thesis, University of Groningen, 2023.

[2] M. Tanabashi *et al.*, "Review of particle physics," *Physical Review D*, vol. 98, 030001, 2018. (Particle Data Group).

[3] R. Mann, *An Introduction to Particle Physics and the Standard Model*. CRC Press, 1st ed., 2009.

[4] N. Arkani-Hamed, T. Han, M. Mangano, and L.-T. Wang, "Physics opportunities of a 100 tev proton-proton collider," *Physics Reports*, vol. 652, pp. 1–49, 2016.

[5] C. Pica, "Beyond the standard model: Charting fundamental interactions via lattice simulations," in *Proceedings of the 34th Annual International Symposium on Lattice Field Theory*, Proceedings of Science, 2017.

[6] P. Aggarwal, A. Borschevsky, M. Denis, K. Esajas, P. A. Haase, Y. Hao, S. Hoekstra, K. Jungmann, T. B. Meijknecht, R. G. Timmermans, L. Willmann, A. Zapara, and NL-eEDM Collaboration, "Measuring the electric dipole moment of the electron in BaF," *The European Physical Journal D*, vol. 72, no. 11, p. 197, 2018.

[7] J. S. M. Ginges and V. V. Flambaum, "Violations of fundamental symmetries in atoms and tests of unification theories of elementary particles," *Physics Reports*, vol. 397, no. 2, pp. 63–154, 2004.

[8] D. J. Gross, "The role of symmetry in fundamental physics," *Proceedings of the National Academy of Sciences*, vol. 93, no. 25, pp. 14256–14259, 1996.

[9] M. Kobayashi and T. Maskawa, "Cp-violation in the renormalizable theory of weak interaction," *Progress of Theoretical Physics*, vol. 49, no. 2, pp. 652–657, 1973.

[10] P. A. B. Haase, D. J. Doeglas, A. Boeschoten, E. Eliav, M. Iliaš, P. Aggarwal, H. L. Bethlem, A. Borschevsky, K. Esajas, Y. Hao, S. Hoekstra, V. R. Marshall, T. B. Meijknecht, M. C. Mooij, K. Steinebach, R. G. E. Timmermans, A. P. Touwen, W. Ubachs, L. Willmann, Y. Yin, and NL-eEDM Collaboration, "Systematic study and uncertainty evaluation of P, T-odd molecular enhancement factors in BaF," *The Journal of Chemical Physics*, vol. 155, no. 3, 034309, 2021.

[11] R. Aaij, B. Adeva, M. Adinol, A. Affolder, Z. Ajaltouni, S. Akar, J. Albrecht, F. Alessio, M. Alexander, S. Ali, G. Alkhazov, P. Alvarez Cartelle, A. A. Alves, S. Amato, S. Amerio, Y. Amhis, L. An, L. Anderlini, J. Anderson, and LHCb Collaboration, "Lhcb detector performance," *International Journal of Modern Physics A*, vol. 30, no. 7, 1530022, 2015.

[12] M. Pospelov and A. Ritz, "Electric dipole moments as probes of new physics," *Annals of Physics*, vol. 318, pp. 119–169, jul 2005.

[13] ACME Collaboration, "Improved limit on the electric dipole moment of the electron," *Nature*, vol. 562, pp. 355–360, 2018.

[14] T. S. R. et al., "An improved bound on the electron's electric dipole moment," *Science*, vol. 381, pp. 46–50, 2023.

[15] N. Fortson, P. Sandars, and S. Barr, "The search for a permanent electric dipole moment," *Physics Today*, vol. 56, no. 6, pp. 33–39, 2003.

[16] K. Jungmann, "Searching for electric dipole moments," *Annalen der Physik*, vol. 525, no. 8-9, pp. 550–564, 2013.

[17] A. Boeschoten, *Precision measurements in diatomic molecules: a route to a permanent electric dipole moment*. PhD thesis, University of Groningen, 2023.

[18] A. Boeschoten, V. R. Marshall, T. B. Meijknecht, A. Touwen, H. L. Bethlem, A. Borschevsky, S. Hoekstra, J. W. F. van Hofslot, K. Jungmann, M. C. Mooij, R. G. E. Timmermans, W. Ubachs, and L. Willmann, "Novel spin-precession method for sensitive edm searches," 2023.

[19] E. Kirilov, W. C. Campbell, J. M. Doyle, G. Gabrielse, Y. V. Gurevich, P. W. Hess, N. R. Hutzler, B. R. O'Leary, E. Petrik, B. Spaun, A. C. Vutha, and D. DeMille, "Shot-noise-limited spin measurements in a pulsed molecular beam," *Phys. Rev. A*, vol. 88, p. 013844, Jul 2013.

[20] V. Marshall, *Spectroscopy and Systematic Effects: an eEDM experiment using BaF molecules*. PhD thesis, University of Groningen, 2024.

[21] J. Baron, W. C. Campbell, D. DeMille, J. M. Doyle, G. Gabrielse, Y. V. Gurevich, P. W. Hess, N. R. Hutzler, E. Kirilov, I. Kozyryev, B. R. O'Leary, C. D. Panda, M. F. Parsons, E. S. Petrik, B. Spaun, A. C. Vutha, and A. D. West, "Order of magnitude smaller limit on the electric dipole moment of the electron," *Science*, vol. 343, p. 269–272, Jan. 2014.

[22] J. Arnaud, *Beam and Fiber Optics*. Academic Press, 1976.

[23] A. E. Siegman, *Lasers*. University Science Books, 1986.

[24] B. Saleh and M. Teich, *Fundamentals of Photonics, 3rd Edition*. 02 2019.

[25] M. Alamo, C. Soncco, R. Helaconde, and A. Gago, "Laser spot measurement using simple devices," *AIP Advances*, vol. 11, p. 075016, 07 2021.

[26] R. Paschotta, "Acousto-optic modulators." RP Photonics Encyclopedia, 2008. Available online: `https://www.rp-photonics.com/acousto_optic_modulators.html`.

[27] Isomet Corporation, *AO Modulation*, 2013. Application Note. Available online: `https://isomet.com/App-Manual_pdf/AO%20Modulation.pdf`.

[28] L. Willmann, Personal communication, June 2025.

[29] S. Kim, *Acousto-optic devices for optical signal processing and quantum computing*. PhD thesis, 2008.

[30] C. Knothe, K. Saroglou, M. Fitton, S. Novelli, and G. Klatt, "High-power single mode fibre coupling." Novanta Photonics Technical Article, 2021. Available online: `https://novantaphotonics.com/high-power-single-mode-fibre-coupling/`.

A Python Code

This appendix presents the code written for modeling the effect of passthrough power fluctuations on the two-photon Rabi frequency as described in section 5.1. Firstly, it performs a Taylor expansion of equation 10 around P_0 to evaluate the sensitivity of Ω_i to power fluctuations. The structure of the code allows for an easy change of P_0 values. A two-dimensional grid of power ratios $\frac{P_E}{P_{E,0}}$ and $\frac{P_F}{P_{F,0}}$ is generated to simulate how realistic variations in the power of each beam jointly affect the normalized two-photon Rabi frequency $\frac{\Omega_{EF}}{\Omega_{EF,0}}$ as described by equation 11. The results of the simulation are shown in figure 16.

```python
import numpy as np
import matplotlib.pyplot as plt
import matplotlib.ticker as ticker

# Constants -> Adapt the average passthrough powers here
P0_E = 0.945
P0_F = 0.945

# Taylor expansion of sqrt(P) around P0
def delta_Omega(P, P0):
    dOmega_dP = 1 / (2 * np.sqrt(P0))
    d2Omega_dP2 = -1 / (4 * P0 ** (3/2))
    delta_P = P - P0
    return dOmega_dP * delta_P + 0.5 * d2Omega_dP2 * delta_P ** 2

# Power ratio arrays -> Adapt the range of the power ratios here
P_over_P0_E = np.linspace(0.9, 1.1, 100)
P_over_P0_F = np.linspace(0.9, 1.1, 100)
E_grid, F_grid = np.meshgrid(P_over_P0_E, P_over_P0_F)

# Compute Omega values
P_E = E_grid * P0_E
P_F = F_grid * P0_F
Omega_E0 = np.sqrt(P0_E)
Omega_F0 = np.sqrt(P0_F)
Omega_E = Omega_E0 + delta_Omega(P_E, P0_E)
Omega_F = Omega_F0 + delta_Omega(P_F, P0_F)
Omega_EF_over_EF0 = (Omega_E * Omega_F) / (Omega_E0 * Omega_F0)

# Plot
fig, ax = plt.subplots(figsize=(12, 8))
contour = ax.contourf(E_grid, F_grid, Omega_EF_over_EF0, levels=50, cmap='
    viridis')

# Colorbar
cbar = plt.colorbar(contour, ax=ax, pad=0.02)
cbar.set_label(r'$\Omega_{EF} / \Omega_{EF,0}$', fontsize=22)
cbar.ax.tick_params(labelsize=20)

# Define ticks
all_ticks = [0.90, 0.925, 0.95, 0.975, 1.00, 1.025, 1.05, 1.075, 1.10]
cbar.set_ticks(all_ticks)
cbar.set_ticklabels([f'{tick:.3f}' for tick in all_ticks])

```

```
# Axes labels and formatting
ax.set_xlabel(r'$P_E / P_{E,0}$', fontsize=22)
ax.set_ylabel(r'$P_F / P_{F,0}$', fontsize=22)
ax.xaxis.set_major_formatter(ticker.FormatStrFormatter('%.3f'))
ax.yaxis.set_major_formatter(ticker.FormatStrFormatter('%.3f'))
ax.tick_params(axis='both', which='major', labelsize=20)

# No grid
ax.grid(False)

plt.tight_layout()
plt.show()
```